EUROPEAN ORGANIZATION FOR NUCLEAR RESEARCH

CERN-EP/82-162
27 October 1982

SPINS, MOMENTS AND CHARGE RADII OF BARIUM ISOTOPES IN THE RANGE $^{122-146}$Ba DETERMINED BY COLLINEAR FAST-BEAM LASER SPECTROSCOPY

A.C. Mueller*), F. Buchinger**), W. Klempt***), E.W. Otten
Institut für Physik, Universität Mainz, Mainz, Fed. Rep. of Germany

R. Neugart
CERN, Geneva, Switzerland

C. Ekström***)
Department of Physics, Chalmers University of Technology, Gothenburg, Sweden

J. Heinemeier
Institute of Physics, University of Aarhus, Aarhus, Denmark

and

The ISOLDE Collaboration, CERN, Geneva, Switzerland

ABSTRACT

Hyperfine structures and isotope shifts of barium isotopes in the mass range 122–146 have been measured in the atomic transition $6s^2\ ^1S_0 \rightarrow 6s6p\ ^1P_1$ (5536 Å), utilizing collinear fast-beam laser spectroscopy at the ISOLDE facility at CERN. Nuclear spins, magnetic dipole and electric quadrupole moments, and the changes of mean square charge radii have been deduced. They are discussed within the framework of current nuclear models, revealing single-particle structure and nuclear-shape variations on both sides of the N = 82 neutron shell closure.

(Submitted to Nucl. Phys. A)

---

*) Present address: GANIL, Caen, France.
**) Present address: Foster Radiation Laboratory, McGill University, Montreal, Quebec, Canada.
***) Present address: CERN, Geneva, Switzerland.

1. INTRODUCTION

The hyperfine structure (hfs) and isotope shift (IS) of atomic spectra have played a key role in the discovery and systematic study of nuclear ground-state spins, electromagnetic moments, and charge radii. Present-day efforts in this field are directed towards a systematic study of long isotopic sequences, including short-lived nuclides far from stability[1]. Owing to the minuteness of the samples of material available from nuclear reactions, these experiments require ultimate sensitivity and specific on-line methods to cope with the short half-lives. In both respects, tuneable dye lasers have opened up new perspectives, also solving the problems of optical resolution, hitherto limited by Doppler broadening.

To date, most of the on-line work with radioactive isotopes, performed at isotope separator facilities, has taken advantage of the special chemical properties of certain elements or groups of elements. The chemically inert mercury and cadmium atoms could be transferred into optical cells[2-4], whereas the ion beams of alkali elements were converted into thermal atomic beams and subjected to optical pumping, magnetic state selection, and sensitive particle detection[5,6].

The present experiment follows the scheme of collinear fast-beam laser spectroscopy, previously applied to neutron-rich rubidium and caesium isotopes at the Mainz reactor[7-9]. This method, avoiding intermediate steps of sample preparation, appears to represent a versatile tool applicable to a variety of elements. As a next step we demonstrate the extension to the atomic spectra of the alkaline earth elements, using barium beams from the ISOLDE on-line isotope separator at CERN. We measured the IS and hfs in the BaI transitions $6s^2\ {}^1S_0 \rightarrow 6s6p\ {}^1P_1$ (5536 Å) for neutron-deficient as well as neutron-rich isotopes, ranging from ^{122}Ba to ^{146}Ba and thus covering almost all known isotopes including some isomeric states. This is a considerable extension of the previous off-line work on stable and longer-lived neutron-deficient isotopes performed by the group at Karlsruhe[10-12].

The experimental procedure and specific requirements of collinear fast-beam laser spectroscopy in combination with on-line isotope separation will be described. The results, including the IS within the full isotopic sequence and the hfs of the odd isotopes, are analysed in terms of the nuclear properties involved. They are characterized by the gradually increasing deformation at both sides of the N = 82 neutron-shell closure.

2. EXPERIMENTAL METHOD

2.1 Principle

Classical optical spectroscopy suffers from the Doppler broadening due to the thermal motion of free atoms. A considerable gain in resolution was achieved by laser methods. This led, in particular, to the first precise barium IS measurements by laser spectroscopy in a collimated atomic beam[10,13]. The remaining drawbacks to ultimate sensitivity for isotopes far from stability are the losses due to a collimation ratio of about 10^{-4} and to the procedure of preparing samples.

In both respects, on-line spectroscopy in the *fast* beam from an isotope separator offers obvious advantages (for an outline of this scheme, see Fig. 3). In collinear geometry, the kinematic compression of the velocity distribution due to acceleration leads to a strong reduction of the Doppler width[14,15]. The acceleration of ions in an electrostatic field leaves their kinetic-energy spread δE unchanged, and since

$$\delta E = mv\delta v \qquad (1)$$

the velocity spread δv decreases inversely proportional to the velocity v. Thus, contrary to other methods, resolution is achieved at no expense in sensitivity. Under favourable conditions, the residual Doppler width may be within the natural line width, allowing all atoms in the beam to be simultaneously excited at resonance. A sufficiently large interaction length enables multiple excitation and spontaneous decay.

The experimental aspects were explored in a study on beams of stable sodium and caesium isotopes[16], with special emphasis on the concept of charge-transfer neutralization of the ion beams. The cross-sections of charge-transfer collisions between alkali ions and atoms in the energy range of a few keV are generally of the order of 10^{-14} cm^2 [17]. This corresponds to impact parameters much larger than atomic radii. Therefore, the momentum transfer is small and the phase-space distribution of the beams remains nearly unchanged. It was shown that collinear-beam spectroscopy on *neutral* atoms can also profit from the Doppler narrowing.

For barium, the charge-transfer reaction with sodium

$$Ba^+ + Na \rightarrow Ba + Na^+ + \Delta E$$

into the atomic ground state is quasi-resonant, ΔE being 72 meV. Therefore, the cross-sections expected are of the order mentioned above, slowly decreasing towards higher beam energies[17]. This gives access to the BaI resonance line at 5536 Å.

The ISOLDE separator, used for the present work, is routinely operated at an acceleration voltage of U = 60 kV. Barium ions emerging from the surface ionization source have an energy spread of the order of 1 eV. The residual Doppler width $\delta\nu_D = \nu_0 \delta v/c$, or

$$\delta\nu_D = \nu_0 \delta E \sqrt{2eUmc^2} \ , \qquad (2)$$

which is equal to about 5 MHz × δE/eV for this particular case ($\nu_0 \simeq 5 \times 10^{14}$ Hz), thus becomes smaller than the natural line width of 19.2 MHz [18].

The beam velocity

$$\beta = v/c = \sqrt{2eU/mc^2} \ *) \qquad (3)$$

(where $\beta \simeq 10^{-3}$) also leads to a considerable Doppler shift

$$\Delta\nu_D = -\nu_0(\beta - \tfrac{1}{2}\beta^2) \ *) \qquad (4)$$

---

*) These formulae are given to the order of β to which the experiment is sensitive.

for the observed optical frequencies, $\Delta\nu_D \simeq 500$ GHz. The frequency in the rest frame of the atoms may thus be varied by changing their velocity, i.e. the acceleration voltage. In this way, the calibration of the laser frequency is replaced by precision measurements of beam energies and energy differences.

2.2 Production and handling of radioactive barium beams

The apparatus is connected to the ISOLDE on-line isotope separator[19] at CERN. Neutron-rich barium isotopes are produced by high-energy fission reactions in a uranium carbide cloth target (15 g/cm^2 of uranium) irradiated with the 600 MeV proton beam of the CERN Synchro-cyclotron at intensities up to 2.4 μA. A 1 μA beam of 910 MeV $^3He^{2+}$ has been used alternatively. The neutron-deficient isotopes are obtained by spallation in a liquid lanthanum target (120 g/cm^2). The reaction products, diffusing out of the hot target container (2200°C for a uranium target, 1300°C for lanthanum) are ionized in a tungsten tube heated to 2400°C. The ions are extracted from the source and accelerated to 60 keV. After electromagnetic mass separation, isobarically pure beams are available in production yields shown in Fig. 1. The quantitative release and ionization of caesium lead to strong isobaric caesium contaminants, which contribute to the background due to their radioactivity.

Special attention is paid to the stability of the acceleration voltage. In order to eliminate this source of line broadening and drift, the high-voltage fluctuations should be kept at a level lower than 10 ppm. Sources of interference are a 50 Hz ripple from the power supplies and 20 kHz from the high-voltage rectifiers, as well as the long-term drift due to temperature and load variations. Load variations are essentially created by the proton beam arriving in bursts of 50 μs at a repetition rate of 170 s^{-1}. Ionization of the ambient air in the target area and the creation of secondary particles in the target give rise to a high pulsed current load on the acceleration voltage, amounting to a peak value of 4 mA per μA mean current of the proton beam. A special stabilization unit has been constructed to eliminate all the disturbing effects. This unit sketched in Fig. 2 operates stepwise. A fast series regulator compensates for the pulsed load and is followed

by a fine regulation[20], subdivided into an a.c. and a d.c. branch. The a.c. error signal, taken out of a capacitive divider, is fed back directly into the regulator whereas the information on the d.c. error, generated at ground level, is communicated via high-frequency modulated light. The current through the highly stable measuring resistor R_0 (< 10 ppm) is compared to that of a constant-current reference standard (< 1 ppm). The whole device ensures an overall stability of better than 0.5 V maximum deviation per day.

Figure 3 gives a schematic view of the apparatus used for collinear fast-beam laser spectroscopy. A parallel-plate deflector bends the ion beam by 10° into the axis defined by the laser beam. The beam is focused on the observation region by an electrostatic quadrupole triplet. Doppler-tuning is accomplished by an acceleration/deceleration voltage applied to the charge-exchange cell. In order to avoid the change of focusing, a system of 5 cylindrical electrodes changes the potential smoothly over a path length of 40 cm in front of the entrance aperture of the cell. The focal length of this system is 16 m for the maximum applied voltage of 5 kV and hence has little influence on the beam divergence.

The charge-exchange cell consists of a 25 cm long stainless-steel tube with a diameter of 25 mm and an aperture of 6 mm at each end. It contains about 3 g of sodium. A vapour pressure of about 10^{-3} Torr is maintained by heating the cell to 250°C in the inner section. The material condensing at the cooled ends ($\sim$ 100°C) is continuously recycled. A secondary electron detector at the exit of the apparatus monitors the intensity of the atomic beam. The shape and the position of the beam are observed on a scanner, which is mounted close to the observation region. In order to optimize the overlap of the laser beam with the atomic beam, a pair of deflectors corrects for small geometrical misalignments before the beam enters the energy-changing system. An overall transmission of 80% (mass separator to end of the apparatus) could be achieved. The efficiency of the charge exchange, which depends on the sodium vapour pressure, can be examined by an additional deflector separating the neutral and the charged components of the beam.

2.3 The observation region

The fluorescence of the excited barium atoms is detected downstream of the charge-exchange cell in the observation region, along a path of 20 cm. The light is collected by a cylindrical mirror and two cylindrical lenses imaging this section of the beam on the 1×20 cm^2 entrance of a light-guide. The latter transforms the intersection to a circle of 2 in. at the output side, fitting it to the shape of the photomultiplier cathode (RCA 8852). The collection efficiency of this system is about 2% of 4π, including losses due to reflection at the surfaces and transmission of the light-guide. The quantum efficiency of the photomultiplier being 10%, the overall detection probability is 2×10^{-3} for the photons emitted from the beam.

For high sensitivity, special attention has to be paid to all sources of background. They include i) the stray light, ii) the dark current of the photomultiplier, iii) the background from radioactivity, and iv) photons from excitational collisions with the rest-gas molecules.

i) Stray light is scattered into the observation region mainly from the exit window and from the apertures of the charge-exchange cell. It is reduced by choosing Brewster windows of high optical quality, taking advantage of the linear polarization of the laser beam. A set of thoroughly blackened apertures with sharp conic edges shields the observation region. Under the best conditions, we observed count rates of 5 kHz stray light per mW of transmitted laser beam. Typical running conditions, however, are 2-5 times higher, since the exit window deteriorated during exposure to the radioactive beam.

ii) Noise from the photocathode is reduced to a dark counting rate of < 300 Hz by cooling the cathode to -30°C.

iii) Radioactivity causes background due to scintillation in the light-guide and ionization in the photomultiplier. As the activities collected on the exit window and the apertures in front of the observation chamber can amount to several curies, the radioactive parts as well as the photon collection system are shielded by 10 cm of lead. The remaining background is kept at a sufficiently low level by avoiding consecutive measurements on high- and low-intensity isotopes.

iv) The light produced by excitation in collisions with rest-gas atoms or molecules (2×10^{-6} Torr) has negligible intensity compared with the fluorescence signals.

2.4 The laser system

The laser system consists of a commercial jet-stream cw dye laser, pumped by an Ar-ion laser. The single-mode output frequency is stabilized by an external temperature-controlled etalon, resulting in a good single-mode stability with a frequency jitter of about 1 MHz and a long-term drift of less than 10 MHz per hour. The rapid disintegration of the dye, rhodamine-110, limits the time of stable operation during data taking to about 12 hours. The laser-beam transport over a distance of 15 m is provided by mirrors and two telescopes, of which the second, with a pinhole for spatial filtering, focuses the beam to a waist of 2-3 mm in the observation chamber. The polarization and intensity of the light can be independently adjusted by a polarization rotator combined with a Glan-Thomson prism. The laser power is monitored at the exit of the apparatus by means of a calorimetric power meter.

2.5 Data acquisition and experiment control

At constant laser frequency, a measurement of the optical line shift between two isotopes requires the knowledge of the velocity $\beta = v/c$ of the respective beams at their resonance [formula (4)]. The corresponding change in acceleration voltage can be expressed to first order by:

$$\frac{\Delta U}{U} = \frac{\Delta m}{m} - \frac{\Delta \nu}{\nu_0} \frac{\sqrt{2mc^2}}{eU} \tag{5}$$

Here, the first term accounts for the change of the mass which requires an additional acceleration of about 450 V per atomic mass unit. The second term, accounting for the change in resonance frequency due to IS and hfs, gives $\Delta U = 230$ V for a shift of 1 GHz. Since the hfs in barium do not exceed 500 MHz, they are covered by a sweep voltage of ±100 V. The wide mass range (122-146) and the large IS of about 500 MHz per neutron number above N = 82, however, require additional offset voltages of several kilovolts.

The sweep voltage is supplied by a programmable voltage source (HP 6131C), controlled by the NOVA 1220 minicomputer (Fig. 3). This sweep floats an adjustable offset voltage of a 10 kV power supply, stabilized to 10 ppm (Fluke 410B). Actually three of these power supplies are used, connected alternately to the acceleration/deceleration system through high-voltage relays. They are controlled by the computer, simultaneously switching the current of the separator magnet. Thus spectra of three different isotopes are recorded in a fast cyclic measuring sequence.

The offset voltages are measured by a 1000:1 divider (absolute accuracy 100 ppm) and a high-precision digital voltmeter (PREMA 6040, absolute accuracy 40 ppm). The constant main acceleration voltage is measured by the precision resistor also used for stabilization (see Section 2.2). The dividing ratio of 10,000:1 is accurate to 100 ppm and stable to better than 10 ppm. The voltages are read out through a CAMAC link into the memory of the mini-computer at regular intervals.

The photomultiplier pulses are amplified, discriminated, and counted in a CAMAC scaler. In the multiscaling measuring program, the scans can be divided into up to 500 channels, and the scanning speed is usually 4 ms per channel. Software commands allow the free choice of scanning parameters separately for each isotope.

3. RESULTS

3.1 Data analysis

Of the three recorded spectra two are taken on reference isotopes, chosen among those for which accurate data are available[11]. The IS between them provide an on-line test of the high-voltage calibration and further systematic errors. The measuring cycle of a number of sweeps for each isotope is continuously repeated until counting statistics are sufficient. Typically, the total measuring time is between 5 min and 1 h. This corresponds to an integration time of up to 10 s per channel. Figure 4 shows the sequence ^{134,140,146}Ba as an example.

The observed resonances have a total line width of about 30 MHz, and exhibit a small asymmetry with a tail towards the low-particle-velocity side of the spectrum. This asymmetry decreases or increases with the sodium vapour pressure in the charge-exchange cell. It can be considerably reduced at the expense of the neutralization efficiency. Similarly, an increase of the rest-gas pressure in the apparatus above several times 10^{-5} Torr leads to more asymmetric shapes. Excitational collisions with very low momentum transfer are considered as an explanation of this behaviour. This has been more clearly seen in a previous experiment on 5 keV caesium beams neutralized in caesium vapour at high pressure. There, the discrete beam-velocity components after multiple excitation could be resolved due the low beam energy and the small natural line width of the optical transition. At the present energy of 60 keV, the discrete steps of kinetic-energy loss are concealed in the natural line width of 19 MHz (corresponding to 4.5 eV and to be compared with excitation energies of about 2 eV). In addition, several excitation channels as well as a quasi-continuous loss by molecular excitation may blur the structure.

The overall effect on the velocity distribution and thus the line shape can be expressed by an exponential function, accounting for the decreasing probability of multiple excitation. Correspondingly, the optical signal $S(\nu)$ in the frequency scale can be written as a convolution of the Lorentzian-shaped resonance line with the exponential function:

$$S(\nu) = N \int_0^\infty e^{-s\nu'} \frac{1}{(\nu-\nu'-\nu_0)^2 + \Gamma^2} \, d\nu' \, , \qquad (6)$$

where s is the slope of the exponential, Γ the width of the Lorentzian, ν_0 the position of the resonance, and N a normalization factor for the strength of the resonance.

A statistical analysis of the observed spectra has been performed by comparing them with $S(\nu)$ in a χ^2 test, assuming pure counting statistics for the photon signal. The parameters of $S(\nu)$ are fitted by minimization of χ^2. The minimization procedure is carried out by the library routine MINUIT of the CERN Cyber 760 computer

system[21]. Examples are given in Fig. 4 (^{134,140,146}Ba), Fig. 5 (^{131,131m}Ba) and Fig. 6 (^{145}Ba), where the solid curves represent the result of the least squares fit. For low laser power (< 100 μW), the line shape is well reproduced by Eq. (6). The FWHM of the Lorentzian is about 21 MHz and the exponential function drops to half its value over 5-10 MHz, corresponding to 1-2 eV. This has to be compared with the natural line width of 19.2(5) MHz [18]. The residual broadening reflects the energy spread of the ion source (< 2 eV, corresponding to 9 MHz), the beam divergence (∿ 2 MHz), and laser-frequency fluctuations (∿ 1 MHz). These contributions are small enough not to distort the symmetric Lorentzian part of the line shape.

3.2 Spin assignments

The relative intensities of the three hyperfine components in the odd-A isotopes exhibit a spin dependence which, in cases of not too high spin values, provides a basis for nuclear-spin assignments. The validity of this procedure has been confirmed by comparing the spectra of the barium isotopes with known spin values. These comparisons have to take into account optical pumping effects and are preferably made within a sequence of isotopes taken in one measuring cycle at low laser power.

The presence of only two hyperfine components in the spectra of ^{125,127}Ba, with intensity ratios equal to those of ^{129,131,133}Ba, for which the spin has already been measured to be I = ½ [11], ascertains the spin assignment I = ½ also for ^{125,127}Ba. Here, the ratios are not affected by optical pumping effects and are therefore close to the theoretical value of 0.4 for π excitation and observation at right angles. Similarly, a spin I = ³⁄₂ is assigned to the nuclide ^{141}Ba on the basis of the intensity ratios, which are equal to those of the stable I = ³⁄₂ nuclei ^{135,137}Ba. Equal spins of I = ⁵⁄₂ have to be assigned to ^{123}Ba and ^{143}Ba, for which the intensity ratios lie between the I = ³⁄₂ cases and those of the I = ⁷⁄₂ nuclei ^{129m}Ba [22] and ^{139}Ba [23]. All these assignments are further supported by the magnitude and sign of the corresponding results for the magnetic dipole and electric quadrupole moments (cf. Section 4.1).

Only two components are observed in the spectrum of ^{145}Ba, but their intensities are not consistent with I = ½. The possibility of missing the weak third component has been excluded by good statistics measurements in comparison with the I = ³⁄₂ isotope ^{137}Ba, performed at low laser power (Fig. 6). We have to assume a coincidence between the strongest and the weakest component, and find the intensities consistent with I = ³⁄₂ which is also suggested by the nuclear moments evaluated under the possible assumptions for I.

Spin assignments for the isomeric states in ^{131}Ba and ^{137}Ba pose problems because of the apparently high spin values and the partial overlap between the ground and isomeric state hfs patterns. Here we adopt the values I = ⁹⁄₂ and I = ¹¹⁄₂, respectively, proposed on the basis of spectroscopic data[24,25].

3.3 Hyperfine constants and isotope shifts

The one-standard-deviation error for the position of a resonance line, as given by the fitting procedure, is usually around 0.5 MHz. For the IS, the digitizing error of the voltmeter measuring the offset voltages (Section 2.5) has to be added; it corresponds to 0.5 MHz in the frequency scale. Comparing several independent measurements for the same sequence of isotopes, one observes an additional statistical scattering of line positions originating from imperfect beam alignment. The angle between the particle and the laser beams may vary by ±1 mrad, corresponding to a shift of 1 MHz.

The systematic error of the frequency shift between the resonances of two isotopes with masses m_1, m_2 ($m \simeq m_1 \simeq m_2$; $\Delta m = m_2 - m_1$) can be derived from Eq. (5). We obtain

$$\delta(\Delta\nu) = \nu_0\left(\frac{eU}{2mc^2}\right)^{\frac{1}{2}}\left\{\frac{1}{2}\left(\frac{\Delta U}{U}+\frac{\Delta m}{m}\right)\frac{\delta U}{U}+\frac{\Delta U}{U}\,\frac{\delta(\Delta U)}{\Delta U}+\frac{\delta m_1}{m}+\frac{\delta m_2}{m}\right\}, \qquad (7)$$

where U and ΔU are the main acceleration voltage and the difference of the post-acceleration voltages, respectively, and δU, $\delta(\Delta U)$, δm_1, δm_2 are the errors on these quantities. The voltage-dependent terms are given by the precision of the measuring voltage dividers (see Section 2.6), $\delta U/U = 10^{-4}$ and $\delta(\Delta U)/\Delta U = 10^{-4}$. The

atomic masses and their errors are taken from the compilation of Wapstra and Bos[26]. Since the voltage differences are mainly determined by the mass-dependent Doppler shift, the voltage uncertainties give a systematic contribution to the error of the IS of about 0.5 MHz × Δm/amu, almost independently of the particular value of the IS. The uncertainty of the atomic masses contributes 2 GHz × δm/amu, which is negligible except for the cases in which calculated values are used and assigned conservative errors of 10^{-3} amu. All these systematic errors are negligible for the hyperfine splittings and isomer shifts.

The new results for the hyperfine constants A and B and the IS are listed in Table 1. For the latter quantity ^{138}Ba serves as common reference, although various reference isotopes were chosen in the measurements. For the evaluation of a consistent set of results, we used the data of Refs. 11 and 12, which are confirmed within our errors and less influenced by systematic contributions. We give the example of ^{124}Ba, where our result $\delta\nu^{138,124}$ = 444(6) MHz is to be compared with 447(1) MHz from Ref. 12. All measured hfs and IS are also plotted in Fig. 7.

4. EXTRACTION OF THE NUCLEAR PARAMETERS

4.1 Nuclear moments

The nuclear electromagnetic moments of the odd-A barium isotopes have been derived from the experimental hyperfine constants using as reference the corresponding known values for the stable isotopes ^{135}Ba and ^{137}Ba [11,27,28].

The magnetic moments are corrected for diamagnetism[25] and assigned an additional error of 0.01 n.m. due to the hfs anomaly. This value, representing an upper limit, is deduced on the basis of the empirical rule of Moskowitz and Lombardi[29] combined with the Z-dependent factor given by Bohr and Weisskopf[30]. The procedure has been checked for the measured hfs anomalies in a number of even-Z elements with 6s6p $^{1,3}P_1$ electron configuration and found to give good estimates. The s-electron contribution to the magnetic hyperfine interaction of the $^1P_1$ state in Ba has been deduced from the analysis in Ref. 18, yielding $\Delta(^1P_1) = 1.87\ \Delta_s$. Because of the uncertainties involved in the evaluation, and particularly in the assignment of

nucleon configurations, we prefer to include a general error rather than corrections for the individual nuclei.

For the spectroscopic quadrupole moments, the analysis of Ma and zu Putlitz[28] has been essentially confirmed by a more recent approach[13] using the empirically modified Breit-Wills theory (see Ref. 18). We use the former values, which are based on the B-factors of several states, and apply the shielding correction factor $1/(1-R_{6p})$ with the value $R_{6p} = -0.23(2)$ given by Sternheimer[31]. Atomic Hartree-Fock calculations including relativistic effects and a semi-empirical estimate of configuration interaction give values about 20% higher[32].

On this basis, a consistent compilation of the magnetic moments and spectroscopic quadrupole moments from all known hfs in barium is given in Table 2.

4.2 Evaluation of $\delta\langle r^2\rangle$

The generally adopted semi-empirical procedure of extracting $\delta\langle r^2\rangle$ from the IS is described in detail by Heilig and Steudel[33]. According to

$$\delta\nu^{AA'} = \delta\nu_f^{AA'} + M\,\frac{A' - A}{A'A} \tag{8}$$

the nuclear recoil-energy contribution (mass shift) has to be subtracted from the measured IS in order to obtain the field shift $\delta\nu_f^{AA'}$. The difference between the mean square nuclear charge radii $\delta\langle r^2\rangle^{AA'}$ is connected with this quantity by

$$\delta\nu_f^{AA'} = F\delta\langle r^2\rangle^{AA'} \tag{9}$$

if the contribution from higher radial moments is neglected.

For the alkaline earth elements, the most reliable values of F should be obtained from s-p transitions in the alkali-like ionic spectra. They are based on the non-relativistic electron density at the nucleus $|\psi(0)|^2$ derived from the ns level sequence or the hyperfine splittings. The relativistic effects are taken into account in the calculation of the IS constant, assuming simple models for the nuclear charge distribution[34], and screening factors from Hartree-Fock calculations are included as corrections. The mass shift should be little influenced by the

correlation of electron momenta ("specific" mass shift) and be close to the "normal" mass shift, $M = \nu_0/1836$.

In this way, Fischer et al.[35] obtained $F_2 = -4890$ MHz/fm^2 for the transition 6s → 6p in Ba II. We follow the procedure of Bekk et al.[11], who extracted the factor $F_1 = 3929$ MHz/fm^2 for the transition $6s^2\ ^1S_0 \rightarrow 6s6p\ ^1P_1$ in Ba I from a King plot of their data and those of Ref. 35, measured in the transition $6s\ ^2S_{1/2} \rightarrow 6p\ ^2P_{1/2}$. We also follow the arguments for the assumption of a zero specific mass shift $M = (1 \pm 1)\nu_0/1836$ in the Ba I transition[33,11].

This analysis relies on a set of ionic IS measured by conventional optical spectroscopy; we measured in addition the IS of all stable barium isotopes in the transition $6s\ ^2S_{1/2} \rightarrow 6p\ ^2P_{3/2}$ in Ba II with a slightly modified collinear-beam apparatus[36]. The results are consistent with the old data, yielding the ratio $F_1(1/2)/F_1(3/2) = 0.971(8)$ between the electronic factors of the field shifts in the two components of the Ba II doublet. The difference between these F factors as well as a small rectification to Babushkin's formula for the IS constant*), is probably less important than the remaining uncertainties in the evaluation of $|\psi(0)|^2$ and the mass shift.

Several recent contributions have thrown light on these problems:

i) Bauche[38] points out that the described procedure of extracting a non-relativistic $|\psi(0)|^2$ from the measured Fermi contact hyperfine interaction gives too large a value because of an under-estimation of the relativistic correction factor taken from the formula of Racah. The alternatively used Goudsmit-Fermi-Segrè formula, giving almost identical results, seems to be appreciably incorrect for heavy atoms. Bauche suggests using correction factors obtained from a comparison between relativistic and non-relativistic Hartree-Fock calculations of the hyperfine structure. For example, this correction would decrease the electronic factor F of CsI by about 12%.

---

*) Zimmermann[37] pointed out that a factor $(n/N)^3$ is missing in the formula and the tabulated values of Ref. 34. For barium, this corresponds to an increase of F by about 4%.

ii) Grundevik et al.[39] performed a consistent relativistic Hartree-Fock calculation of the electronic factors F in a number of Ba I and Ba II transitions. Their result for F_1 is more than 30% smaller than the semi-empirical value. This follows the trend of earlier non-relativistic Hartree-Fock calculations of $|\psi(0)|^2$ (see Refs. 35 and 33).

iii) Recently published muonic data[40] yield $F_1 = -3035(260)$ MHz/fm^2 and a small total mass-shift constant M = 5(11) MHz. However, these results seem to be in disagreement with the as yet unpublished ones of Simons et al.[41] which tend to be more consistent with the conventional analysis of the optical data. Irrespective of this discrepancy, both experiments confirm the assumption that the specific mass shift should at most be of the order of the normal mass shift.

Since none of these approaches is conclusive at the present stage, we prefer to remain consistent with the values of Bekk et al.[11] for barium and with the systematics of $\delta\langle r^2\rangle$ from optical IS [33], in particular for comparisons with the neighbouring elements caesium and xenon. The results for the full sequence of isotopes are included in the compilation of Table 2. For $N < 82$, where the IS are small, the errors are dominated by the uncertainty of the specific mass shift, increasing roughly from 20 to 40% with distance from the reference isotope ^{138}Ba. This contribution is negligible for $N > 82$, where the error of F_1 dominates. Notwithstanding the discussion above, the semi-empirical analysis is supported by its general success in yielding consistent information on the behaviour of nuclear radii over a large range of the chart of nuclides[33]. Significant deviations of more than about 10% would also disturb the consistent picture of mean square radii and nuclear deformation (cf. Section 5.2), particularly in regions where $\delta\langle r^2\rangle$ is large. In any case, the structure of the $\delta\langle r^2\rangle$ curve and the relative changes are not touched by the scaling uncertainty.

5. DISCUSSION

The knowledge of nuclear spins, moments, and charge radii in the barium isotopes now covers the wide range from ^{122}Ba to ^{146}Ba. The present work has included not only neutron-deficient nuclides, but also a number of neutron-rich ones above the neutron-shell closure at N = 82 *). It is thus possible to follow the variation of nuclear deformation and single-particle structure as neutrons are subtracted from or added to the closed shell. Previously, laser spectroscopy on the longer-lived neutron-deficient isotopes[11] has supported the picture of increasing quadrupole deformation and decreasing triaxiality towards the lighter nuclides, as suggested by the analysis of the level structure of the even[44] and odd[45] barium isotopes.

Firstly, we shall discuss the spins and moments of the odd isotopes. Certainly, it is not obvious which model may account best for the nuclear properties in this transitional region. Here, we have chosen a core-quasiparticle approach[46], based on the Nilsson model. This has been shown to be remarkably successful in the interpretation of nuclear spins and moments over a wide range of different nuclei, including species with strongly deformed nuclear shapes as well as weakly deformed ones[47]. Secondly, we shall discuss the information on the nuclear deformation extracted from the mean square charge radii.

5.1 Spins and moments

The single-particle levels relevant in the present discussion are shown in the Nilsson diagram of Fig. 8. The energy of the orbitals originating from the shell-model states $d_{5/2}$, $g_{7/2}$, $h_{11/2}$, $s_{1/2}$ and $d_{3/2}$ below N = 82, and from $f_{7/2}$, $h_{9/2}$ and $i_{13/2}$ above N = 82, are plotted versus the deformation parameter β. In addition, Fig. 8 contains the Fermi levels of the sequence of odd-N barium isotopes $^{123-145}$Ba. The influence of the γ-deformation on the energy levels between 0° and 30° is given in the right side of the figure for β = 0.22. Generally, the choice of γ-angle has little influence on the theoretical nuclear moments, in contrast to the

---

*) An isotope-shift measurement for ^{140}Ba in the transition 5d $^2D_{3/2}$ → 6p $^2P_{3/2}$ of Ba II has been reported by Silverans et al.[42], in parallel with the first results of this experiment[43]. Both measurements are consistent and in disagreement with the previously reported result of Ref. 35.

substantial improvement in the nuclear level structure achieved in a number of cases by choosing $\gamma \neq 0$.

Comparisons between experimental and calculated nuclear moments are presented in Fig. 9 (the ground states of $^{125-137}$Ba), Fig. 10 (the ground state of ^{123}Be and the isomeric states of $^{129-137}$Ba), and Fig. 11 (the ground states of the neutron-rich isotopes $^{139-145}$Ba). The effective neutron g-factors, $g_s = 0.6\ g_s^{free}$, $g_\ell = 0$, and $g_R = Z/A$, have been used in the calculation of the magnetic dipole moments.

Below N = 82, there are first the weakly deformed $I^\pi = 3/2^+$ nuclei ^{137,135}Ba with a main contribution from [402 3/2], being a rather pure $(d_{3/2})_{3/2}$ shell-model state. The lowering of the Fermi level and the increase in deformation explain well the gradual change from large negative to small positive magnetic moments in the sequence of the succeeding spin I = 1/2 isotopes $^{133-125}$Ba. The nuclei ^{133,131}Ba are mainly associated with the orbital [400 1/2], ^{127,125}Ba with [411 1/2], and ^{129}Ba with a combination of both. A γ-angle of about 20° has to be introduced to reproduce the spin 1/2 ground state in the full sequence. This may be understood from Fig. 8 in which the orbital [400 1/2] is sloping down with increasing γ-deformation while [411 1/2] is sloping up, thus covering the range $^{133-125}$Ba. A similar triaxiality has to be used to get the orbital [402 5/2] close to the Fermi level of ^{123}Ba. The experimental nuclear moments clearly indicate a [402 5/2] assignment to this nucleus.

A good agreement between experiment and calculations is also found for the nuclear moments of the isomeric states in $^{129-137}$Ba; the main components of the nuclear wave functions being [404 7/2] in ^{129m}Ba, [514 9/2] in ^{131m}Ba, and [505 11/2] in the remaining isomers ^{133m,135m,137m}Ba.

The neutron-rich barium isotopes above N = 82 may be interpreted, assuming prolate nuclear shapes, in terms of the low-Ω orbitals originating from the $f_{7/2}$ and $h_{9/2}$ shell-model states (see Fig. 8). A gradual increase of deformation is suggested by the nuclear moments, as indicated also by the IS data and by the energy-level systematics[48].

The wave function of the weakly deformed $^{7}/_{2}^{-}$ ground state of ^{139}Ba follows essentially the rotation-aligned coupling scheme and is, within the particle-rotor approach, built up mainly of the orbitals $[541\ ^{1}/_{2}]$ and $[532\ ^{3}/_{2}]$, which in turn to a large extent are due to $(f_{7/2})_{1/2}$ and $(f_{7/2})_{3/2}$, respectively. This composition of the wave function is reflected particularly in the spectroscopic quadrupole moment, in which the negative sign arises from the projection of the positive intrinsic quadrupole moment Q_0,

$$Q_s = Q_0 \frac{3\sum_{\nu,\Omega}\left(a_{\Omega}^{I\nu}\right)^2 - I(I+1)}{(I+1)(2I+3)}, \qquad (10)$$

since $\Omega < I$. Here $a_{\Omega}^{I\nu}$ are the expansion coefficients of the Nilsson orbitals ν contributing to the total wave function.

The positive quadrupole moments of the $I = {}^{3}/_{2}$ nuclei ^{141}Ba and ^{145}Ba, on the other hand, indicate a wave function built up of $\Omega = I$ orbitals. In the particle-rotor calculation, an $I^{\pi} = {}^{3}/_{2}^{-}$ state, originating mainly from $[532\ ^{3}/_{2}]$ in ^{141}Ba and from $[532\ ^{3}/_{2}]$ and $[521\ ^{3}/_{2}]$ in ^{145}Ba, is obtained at low excitation energy for deformations $\beta \simeq 0.22$-0.27. The $I^{\pi} = {}^{5}/_{2}^{-}$ ground state of ^{143}Ba is represented by a mixture of low-Ω orbitals from $f_{7/2}$ and $h_{9/2}$, the dominant components at $\beta \simeq 0.22$-0.27 being $[530\ ^{1}/_{2}]$ and $[532\ ^{3}/_{2}]$.

As shown above, the experimental nuclear moments for the full sequence of odd-A barium isotopes are well accounted for by the core-quasiparticle model[46]. The main components of the nuclear wave functions have been derived, consistent with a gradual increase in deformation on both sides of the N = 82 neutron-shell closure. Information on the nuclear deformation is also obtained from the experimental charge radii, suggesting a direct comparison with the preceding conclusions.

5.2 Mean square charge radii

Figure 12 contains a plot of the change in mean square charge radii $\delta\langle r^2\rangle$ with respect to ^{138}Ba versus the neutron number N. The influence of the shell structure is clearly visible as an abrupt change in the slope at N = 82. Such a

behaviour has been interpreted as the superposition of a smoothly varying part, describing nuclear charge radii with a constant spherical shape and a change of $\langle r^2 \rangle$ due to deformation, according to

$$\langle r^2 \rangle = \langle r^2 \rangle_0 \left(1 + \frac{5}{4\pi} \langle \beta^2 \rangle\right) \tag{11}$$

where $\langle r^2 \rangle_0$ is the mean square radius of the corresponding spherical nucleus with the same volume and β is the quadrupole deformation parameter[49,50]. We have not taken into account contributions from higher-order multipoles. This approach will be shown to fit the data fairly well.

For ^{138}Ba, $\langle r^2 \rangle$ = 23.3481(34) fm^2 can be taken from the muonic data[40], and β = 0.090(1) has been derived from the reduced B(E2) transition probability[51]. Choosing the droplet model of Myers[52] to describe the change in the spherical contribution, one obtains the absolute mean square deformations from $\delta\langle r^2 \rangle$ values by the use of formula (10). These values of $\langle \beta^2 \rangle^{1/2}$ are plotted in Fig. 13 versus the neutron number. The curve shows a fairly monotonic increase of the deformation above N = 82, up to N = 90, as well as a continuation of the trend for N < 82 towards more neutron-deficient isotopes. Figure 13 contains also the deformations known from B(E2) reduced transition probabilities[51]. The good consistency of the information from IS and B(E2) has already been observed, for N < 82, by Bekk et al.[11] and earlier by Ullrich and Otten[50]. For the most strongly deformed nuclei, ^{123}Ba and ^{145}Ba, the deformation parameters β = 0.26 and 0.25, respectively, have been derived from the spectroscopic quadrupole moments (see Figs. 10 and 11). These cases correspond essentially to the strong-coupling limit of pure Nilsson states with the sum in formula (10) replaced by $\Omega^2 = I^2$. The agreement of this independent information with the IS data on both sides of the neutron-shell closure supports again the quantitative relevance of the picture and thus the conventional choice of F in the evaluation of $\delta\langle r^2 \rangle$. On the other hand, it confirms the general success of the droplet model in describing the change of mean square charge radii with neutron number by the neutron skin effect. In the earlier literature, this deviation from the so-called $A^{1/3}$ law has been described by an empirical parameter ("IS discrepancy").

The behaviour of $\delta\langle r^2\rangle$ of the neighbouring elements Xe, Cs and Ba, also compared in Fig. 12, is remarkably similar. The Z-dependence of $\delta\langle r^2\rangle$ and thus β points to the influence from the proton-shell closure at Z = 50, notwithstanding the systematic uncertainties in the calculation of $\delta\langle r^2\rangle$ for different elements.

Another, microscopic, approach to the nuclear charge radii can be made by Hartree-Fock calculations, using a density-dependent force between the nucleons (DDHF) [53]. The results of such a calculation[54] (Fig. 14) reproduce the experimental data above N = 82. Below, however, they predict unrealistically weak deformations. This discrepancy, already observed for the case of Rb [55], can, at least partly, be attributed to the static character of deformation in the DDHF calculation, not taking into account the zero-point quadrupole vibrations.

Predictions from the interacting-boson model, available for $N < 82$ [56], are in good agreement with the IS data. This approach, however, will not give a coherent description of $\delta\langle r^2\rangle$ across the neutron-shell closure, because it implies an independent set of parameters for the neutron-rich isotopes.

Since these calculations and comparisons are restricted to even isotopes, they miss the pronounced effect of odd-even staggering, clearly recognized in Fig. 12 for the neutron-deficient isotopes. For the neutron-rich isotopes this effect is hidden in the steep slope of the $\delta\langle r^2\rangle$ curve. The staggering has been interpreted only qualitively in a pairing-plus-quadrupole model which gives evidence that the mean square deformation $\langle\beta^2\rangle$ associated with zero-point quadrupole vibrations is greater for even than for odd isotopes[57]. New ideas should be developed for a more general and quantitative understanding of this effect which is equally important in the regions of almost spherical and strongly deformed nuclear shapes. Here, it may be worth noting that the absolute staggering (i.e. the difference in $\delta\langle r^2\rangle$ between the odd isotope and the average of its even neighbours) is of the same order of magnitude for all isotopes with $N < 82$, but decreases to zero within the sequence $82 < N < 90$.

6. CONCLUDING REMARKS

The present experiment has considerably extended the knowledge of spins, moments, and charge radii in barium, allowing a systematic mapping of nuclear structure and shape on both sides of the neutron-shell closure at N = 82. The analysis of the nuclear spins and moments, performed within a nuclear core-quasiparticle approach based on the Nilsson model, has permitted a determination of the main components of the nuclear wave functions. These data are consistent with a gradual increase in nuclear quadrupole deformation on both sides of N = 82, as determined from the variation in charge radii.

The strong resonance transition $^1S_0 \rightarrow {}^1P_1$ in Ba I is certainly one of the most favourable examples of the sensitivity of collinear fast-beam laser spectroscopy. An ultimate sensitivity limit of some 10^4 atoms/s for even isotopes has been established. We consider the very neutron-rich ^{148}Ba and the very neutron-deficient ^{120}Ba to be within the reach of well-optimized running conditions of the ISOLDE separator. The versatility of the method is presently exploited for a more systematic mapping of charge radii and moments in the transitional region between N = 82 and strong deformation for the neutron-deficient isotopes of the heavier rare earths[58].

Acknowledgements

We would like to thank K.-H. Georgi and B. Vosicki for their pioneering efforts in the development of the high-voltage stabilization. We also acknowledge the very valuable help of E. Chauchard, B. Schinzler, W. Stampp and K. Wendt. The quality of the mechanical and electronic components, built by the workshops of Mainz University, has ensured the performance of our apparatus. We would like to thank all CERN staff whose professional skill has enabled us to carry out these experiments.

This work was supported by the Deutsche Forschungsgemeinschaft and the Bundesministerium für Forschung und Technologie.

REFERENCES

1) E.W. Otten, Nucl. Phys. A354 (1981) 471c.

2) G. Huber, J. Bonn, H.J. Kluge and E.W. Otten, Z. Phys. A276 (1976) 187.

3) P. Dabkiewicz, G. Buchinger, H. Fischer, H.J. Kluge, H. Kremmling, T. Kühl, A.C. Mueller and H.A. Schuessler, Phys. Lett. 82B (1979) 199.

4) F. Buchinger, P. Dabkiewicz, H.J. Kluge, A.C. Mueller and E.W. Otten, Hyperfine Interactions 9 (1981) 165.

5) G. Huber, F. Touchard, S. Büttgenbach, C. Thibault, R. Klapisch, H.T. Duong, S. Liberman, J. Pinard, J.L. Vialle, P. Juncar and P. Jacquinot, Phys. Rev. C18 (1978) 2342.

6) C. Thibault, F. Touchard, S. Büttgenbach, R. Klapisch, M. de Saint-Simon, H.T. Duong, P. Jacquinot, P. Juncar, S. Liberman, P. Pillet, J. Pinard, J.L. Vialle, A. Pesnelle and G. Huber, Nucl. Phys. A367 (1981) 1.

7) B. Schinzler, W. Klempt, S.L. Kaufman, H. Lochmann, G. Moruzzi, R. Neugart, E.W. Otten, J. Bonn, L. von Reisky, K.P.C. Spath, J. Steinacher and D. Weskott, Phys. Lett. 79B (1978) 209.

8) J. Bonn, W. Klempt, R. Neugart, E.W. Otten and B. Schinzler, Z. Phys. A289 (1979) 227.

9) W. Klempt, J. Bonn and R. Neugart, Phys. Lett. 82B (1979) 47.

10) G. Nowicki, K. Bekk, S. Göring, A. Hanser, H. Rebel and G. Schatz, Phys. Rev. C18 (1978) 2369.

11) K. Bekk, A. Andl, S. Göring, A. Hanser, G. Nowicki, H. Rebel and G. Schatz, Z. Phys. A291 (1979) 219.

12) H. Rebel, K. Bekk, G. Nowicki and G. Schatz, Nukleonika 25 (1980) 145.

13) P.E.G. Baird, R.J. Brambley, K. Burnett, D.N. Stacey, D.M. Warrington and G.K. Woodgate, Proc. R. Soc. London Ser. A 365 (1979) 567.

14) S.L. Kaufman, Opt. Commun. 17 (1976) 309.

15) W.H. Wing, G.A. Ruff, W.E. Lamb, Jr. and J.J. Spezeski, Phys. Rev. Lett. 36 (1976) 1488.

16) K.R. Anton, S.L. Kaufman, W. Klempt, G. Moruzzi, R. Neugart, E.W. Otten and B. Schinzler, Phys. Rev. Lett. 40 (1978) 642.

17) H.S.W. Massey and H.B. Gilbody, Electronic and ionic impact phenomena (Clarendon Press, Oxford, 1974), Vol. 4.

18) H.-J. Kluge and H. Sauter, Z. Phys. 270 (1974) 295.

19) H.L. Ravn, Phys. Rep. 54 (1979) 201.

20) K.H. Georgi, Nucl. Instrum. Methods 186 (1981) 271.

21) F. James and M. Roos, Comput. Phys. Commun. 10 (1975) 343.

22) J. Gizon, A. Gizon and J. Meyer-ter-Vehn, Nucl. Phys. A277 (1977) 464.

23) L.K. Peker, Nucl. Data Sheets 32 (1981) 1.

24) J. Gizon, A. Gizon and D.J. Horen, Nucl. Phys. A252 (1975) 509.

25) V.S. Shirley and C.M. Lederer, Table of nuclear moments, *in* Table of isotopes (Wiley, New York, 1978), 7th edn.

26) A.H. Wapstra and K. Bos, At. Data Nucl. Data Tables 19 (1977) 177.

27) L. Olschewski, Z. Phys. 249 (1972) 205.

28) I.-J. Ma and G. zu Putlitz, Z. Phys. A277 (1976) 107.

29) P.A. Moskowitz and M. Lombardi, Phys. Lett. 46B (1973) 334.

30) A. Bohr and V.F. Weisskopf, Phys. Rev. 77 (1950) 94.

31) R.M. Sternheimer, private communication.

32) G. Olsson, private communication.

33) K. Heilig and A. Steudel, At. Data Nucl. Data Tables 14 (1974) 613.

34) F.A. Babushkin, Zh. Eksp. Teor. Fiz. 44 (1963) 1661 [English transl. Sov. Phys.-JETP 17 (1963) 1118].

35) W. Fischer, M. Hartmann, H. Hühnermann and H. Vogg, Z. Phys. 267 (1974) 209.

36) K. Wendt, F. Buchinger, W. Klempt, A.C. Mueller, R. Neugart and E.W. Otten, Isotope shift and hyperfine structure in the transition 6s $^2S_{1/2}$ → 6p $^2P_{3/2}$ of Ba II, to be published.

37) D. Zimmermann, private communication.

38) J. Bauche, Comments Atom. Mol. Phys. 10 (1981) 57.

39) P. Grundevik, private communication.

40) E.B. Shera, J.D. Wohlfahrt, M.V. Hoehn and Y. Tanaka, Phys. Lett. 112B (1982) 124.

41) L.M. Simons, private communication.

42) R.E. Silverans, G. Borghs and J.-M. Van den Cruyce, Hyperfine Interactions 9, (1981) 193.

43) R. Neugart, F. Buchinger, W. Klempt, A.C. Mueller, E.W. Otten, E. Ekström and J. Heinemeier, Hyperfine Interactions 9 (1981) 151.

44) D. Habs, H. Klewe-Nebenius, K. Wisshak, R. Löhken, G. Nowicki and H. Rebel, Z. Phys. 267 (1974) 149.

45) J. Gizon and A. Gizon, Z. Phys. A285 (1978) 259.

46) S.E. Larsson, G. Leander and I. Ragnarsson, Nucl. Phys. A307 (1978) 189.

47) C. Ekström, Proc. 4th Int. Conf. on Nuclei far from Stability, Helsingør, 1981, CERN 81-09 (1981), p. 12.

48) S.M. Scott, W.D. Hamilton, P. Hungerford, D.D. Warner, G. Jung, K.D. Wünsch and B. Pfeiffer, J. Phys. G 6 (1980) 1291.

49) D.N. Stacey, Rep. Prog. Phys. 29 (1966) 171.

50) S. Ullrich and E.W. Otten, Nucl. Phys. A248 (1975) 173.

51) P.M. Endt, At. Data Nucl. Data Tables 26 (1981) 47.

52) W.D. Myers, Phys. Lett. 30B (1969) 451.

53) X. Campi, H. Flocard, A.K. Kerman and S. Koonin, Nucl. Phys. A251 (1975) 193.

54) M. Epherre, G. Audi and X. Campi, Proc. 4th Int. Conf. on Nuclei far from Stability, Helsingør 1981, CERN 81-09 (1981), p. 62.

55) X. Campi and M. Epherre, Phys. Rev. C 22 (1980) 2605.

56) G. Puddu, O. Scholten and T. Otsuka, Nucl. Phys. A348 (1980) 109.

57) B.S. Reehal and R.A. Sorensen, Nucl. Phys. A161 (1971) 385.

58) R. Neugart, Proc. Int. Conf. on Lasers in Nuclear Physics, Oak Ridge, 1982, to be published in Vol. 3, Nuclear Science Research Conference Series, Harwood Academic Publishers, 1982.

Table 1

Experimental results on nuclear spins, hyperfine constants and isotope shifts. The isotope shifts are all given relative to ^{138}Ba.

Mass number	Nuclear spin I	Hyperfine constants A (MHz)	Hyperfine constants B (MHz)	Isotope shift IS (MHz)
122	0			521(7)
123	5/2	48.3(5)	334.0(2.0)	603(9)
125	1/2	-62.2(5)		491(6)
127	1/2	-31.4(5)		436(5)
131m	9/2	34.0(3)	321(8)	264(3)
137m	11/2	31.7(5)	171(14)	-31(2)
139	7/2	49.0(3)	-110.2(1.8)	-473(3)
140	0			-1075(3)
141	3/2	40.6(7)	94.2(1.5)	-1505(5)
142	0			-2019(4)
143	5/2	-31.9(7)	-177.4(2.5)	-2494(8)
144	0			-3025(10)
145	(3/2)	44.5(1.8)	178(4)	-3407(9)
146	0			-3887(11)

Table 2

Summary of nuclear moments and changes in mean square charge radii of $^{122-146}$Ba, evaluated from the experimental data of this work (Table 1) and those of the Karlsruhe Group[11,12].

Mass number	Nuclear spin I	Nuclear moments		$\delta\langle r^2\rangle$
		μ (n.m.)	Q_s (b)	(10^{-2} fm^2)
122				-20.4
123	5/2	-0.687(18)	1.52(13)	-22.0
124				-17.5
125	1/2	0.177(12)		-18.2
126				-14.2
127	1/2	0.089(12)		-15.8
128				-11.1
129	1/2	-0.398(16)		-11.8
129m	7/2	0.930(17)	1.60(13)	-13.0
130				-8.6
131	1/2	-0.709(16)		-9.3
131m	9/2	-0.870(18)	1.46(13)	-9.6
132				-6.8
133	1/2	-0.777(14)		-8.4
133m	11/2	-0.910(51)	0.89(7)	-7.2
134				-5.3
135	3/2	0.837943(17)	0.146(16)	-7.9
135m	11/2	-1.001(15)	0.96(8)	-5.3
136				-4.1
137	3/2	0.937365(20)	0.228(24)	-5.9
137m	11/2	-0.992(26)	0.78(9)	0.4
138				0
139	7/2	-0.975(17)	-0.50(4)	12.4
140				28.1
141	3/2	-0.346(16)	0.43(4)	39.5
142				52.9
143	5/2	0.454(20)	-0.81(7)	65.4
144				79.3
145	(3/2)	-0.380(25)	0.81(7)	89.3
146				101.9

Figure captions

Fig. 1 : ISOLDE production yields of barium and caesium from 600 MeV proton-induced reactions in a 120 g/cm^2 lanthanum target and a 15 g/cm^2 uranium target. The curves are normalized to a proton current of 1 μA.

Fig. 2 : Block diagram of the ISOLDE high-voltage stabilization system, partly designed for this experiment. The precision regulator part has been described in detail by Georgi[20].

Fig. 3 : Schematic view of the experimental set-up including the ISOLDE mass separator and the apparatus for collinear-beam spectroscopy. A simplified block diagram of the electronics, and of the control and data-taking systems is given at the bottom.

Fig. 4 : Fluorescence signal as a function of the acceleration voltage, recorded in a measuring cycle on ^{134}Ba, ^{140}Ba, and ^{146}Ba. The integration time per channel was 0.36 s, 1 s, and 36 s, respectively. The solid curve is the result of the fitting procedure described in the text.

Fig. 5 : Hyperfine structure of the I = $^3/_2$ ground state and the I = $^{11}/_2$ isomeric state in ^{137}Ba. The components are denoted by the quantum number F in the excited $^1P_1$ state.

Fig. 6 : Hyperfine structure spectrum of ^{145}Ba. As discussed in the text, a nuclear spin assignment of I = $^3/_2$ and overlapping F = $^5/_2$ and F = $^1/_2$ components offer a consistent interpretation of the spectrum.

Fig. 7 : Positions of the hyperfine components (dashes) and their centres of gravity (circles) in the Ba I line 5536 Å for the sequence of isotopes $^{122-146}$Ba. The figure includes the data from this work (indicated by arrows) and those of the Karlsruhe group[11,12]. Nuclear spin assignments are given at the top.

Fig. 8 : Nilsson diagram for odd neutrons calculated with the potential parameters $\kappa = 0.0665$ and $\mu = 0.435$. The Fermi levels of the odd-A isotopes $^{123-145}$Ba are indicated by wavy lines. The down-sloping negative-parity states in the upper part of the figure are due to the shell-model states $2f_{7/2}$ and $1h_{9/2}$ above N = 82. The right part of the figure shows the influence of the asymmetry parameter γ on the energy levels at the deformation $\beta = 0.22$.

Fig. 9 : Experimental nuclear moments (horizontal lines) in comparison with the results from particle-rotor calculations for the odd-A isotopes $^{125-137}$Ba. The theoretical curves of the $I = 1/2$ isotopes ^{131,133}Ba and ^{125,127}Ba are mainly due to the orbitals $[400\ 1/2]$ and $[411\ 1/2]$, respectively, while that of ^{129}Ba is a mixture of both.

Fig. 10 : Experimental nuclear moments (horizontal lines) in comparison with the results from particle-rotor calculations for ^{123}Ba and the isomeric states in $^{129-137}$Ba. The main components are due to $[402\ 5/2]$ in ^{123}Ba, $[404\ 7/2]$ in ^{129m}Ba, $[514\ 9/2]$ in ^{131m}Ba, and the upper sublevels from $h_{11/2}$ in the less deformed ^{133m,135m,137m}Ba.

Fig. 11 : Experimental nuclear moments (horizontal lines) in comparison with the results from particle-rotor calculations for the isotopes in the region N > 82. The main components are due to sublevels from the $f_{7/2}$ and $h_{9/2}$ shell-model states. The weakly deformed ^{139}Ba is represented mainly by $f_{7/2}$, while the moments of ^{141}Ba and ^{145}Ba indicate an association with a rather pure $[532\ 3/2]$ Nilsson-model state.

Fig. 12 : Change of mean square charge radii $\delta\langle r^2\rangle$ in the isotopic sequences $^{122-146}$Ba (Refs. 11 and 12 and this work), $^{118-145}$Cs (Ref. 6) and $^{124-136}$Xe (Ref. 33). The change in deformation $\delta\langle\beta^2\rangle^{1/2}$, with respect to N = 82, is indicated by the parallel lines, the slope of which is given by the droplet model.

Fig. 13 : Nuclear deformation $(\beta^2)^{\frac{1}{2}}$ derived from the IS data in the sequence $^{122-146}$Ba ($66 \leq N \leq 90$). The values derived from reduced B(E2) transition probabilities[51] (open squares) are included for comparison.

Fig. 14 : Comparison between the experimental charge radii and the theoretical ones calculated by DDHF[53,54]. The straight solid line shows the behaviour of the spherical part of the charge radii as given by the droplet model[52].

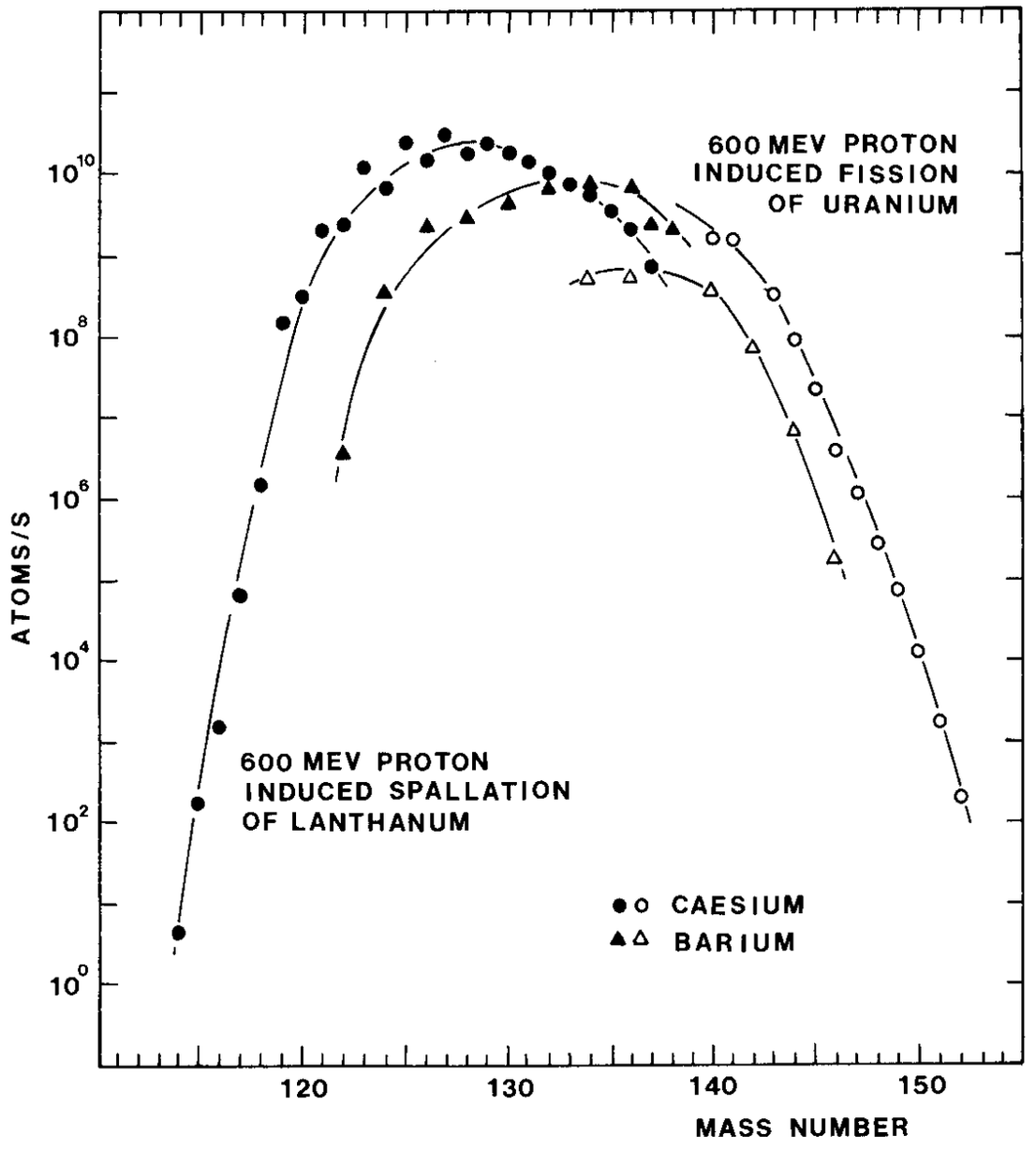
600 MEV PROTON
INDUCED FISSION
OF URANIUM
600 MEV PROTON
INDUCED SPALLATION
OF LANTHANUM
CAESIUM
BARIUM
ATOMS/S
MASS NUMBER
10^{10}
10^{8}
10^{6}
10^{4}
10^{2}
10^{0}
120
130
140
150

Fig. 1

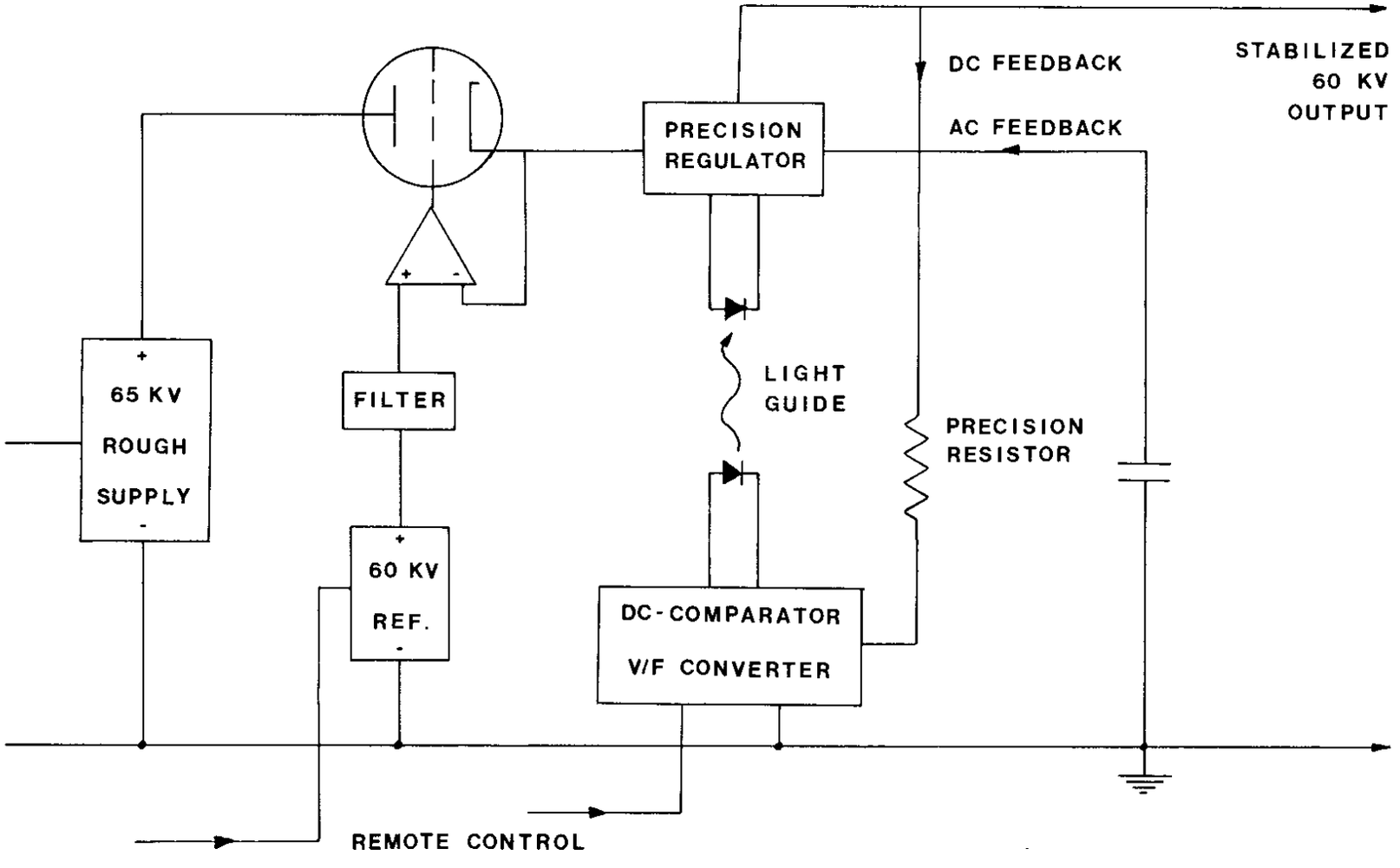
STABILIZED
60 KV
OUTPUT
DC FEEDBACK
AC FEEDBACK
PRECISION
REGULATOR
+
-
+
65 KV
ROUGH
SUPPLY
-
FILTER
LIGHT
GUIDE
PRECISION
RESISTOR
+
60 KV
REF.
-
DC-COMPARATOR
V/F CONVERTER
REMOTE CONTROL

Fig. 2

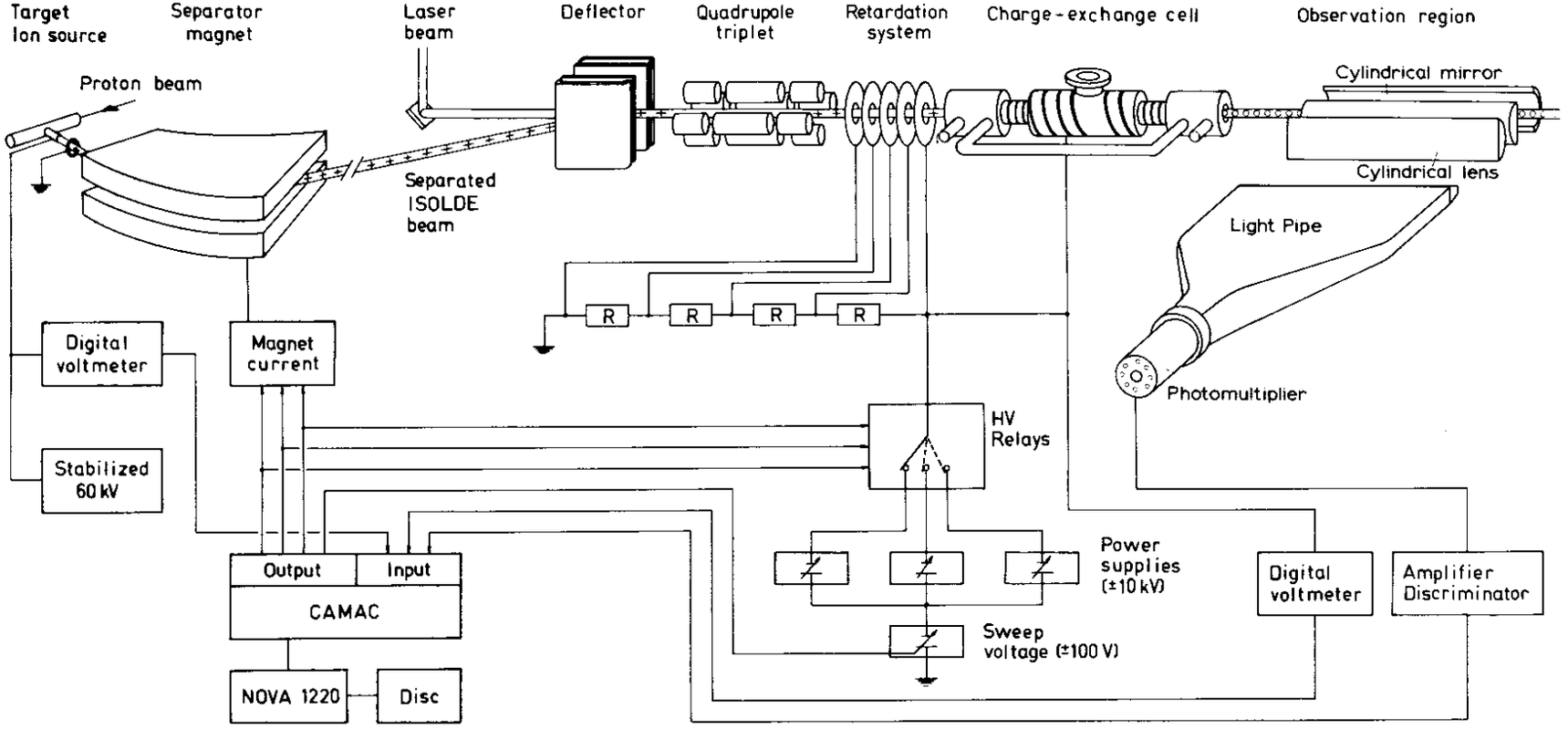
Target
Ion source
Separator
magnet
Laser
beam
Deflector
Quadrupole
triplet
Retardation
system
Charge-exchange cell
Observation region
Proton beam
Separated
ISOLDE
beam
Cylindrical mirror
Cylindrical lens
Light Pipe
Photomultiplier
R
R
R
R
Digital
voltmeter
Magnet
current
Stabilized
60 kV
HV
Relays
Output
Input
CAMAC
NOVA 1220
Disc
Power
supplies
(±10 kV)
Sweep
voltage (±100 V)
Digital
voltmeter
Amplifier
Discriminator

Fig. 3

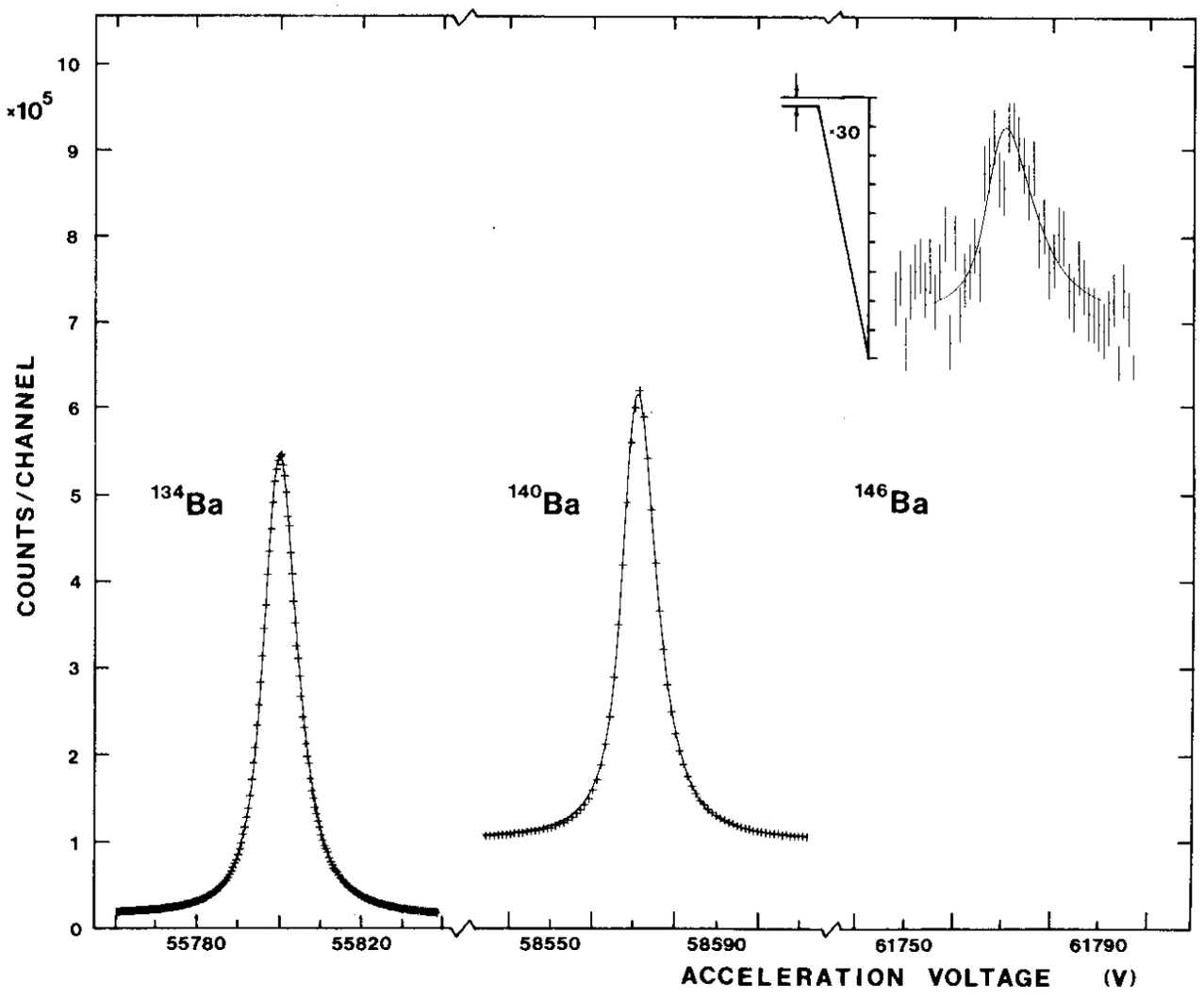
×10^5
COUNTS/CHANNEL
10
9
8
7
6
5
4
3
2
1
0
·30
134Ba
140Ba
146Ba
55780
55820
58550
58590
61750
61790
ACCELERATION VOLTAGE (V)

Fig. 4

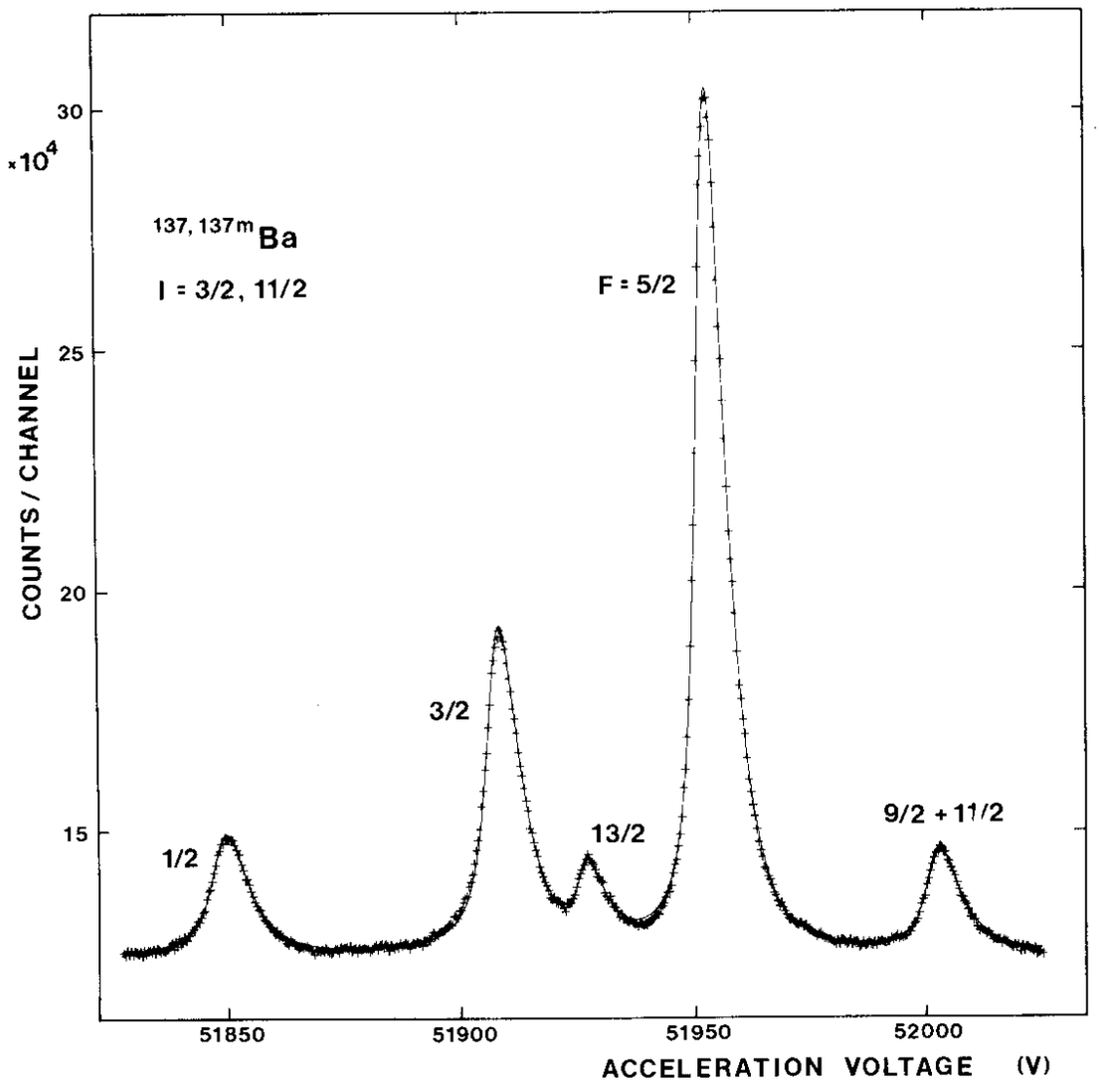
30
×10^4
137, 137m Ba
I = 3/2, 11/2
F = 5/2
25
COUNTS / CHANNEL
20
3/2
15
1/2
13/2
9/2 + 11/2
51850
51900
51950
52000
ACCELERATION VOLTAGE (V)

Fig. 5

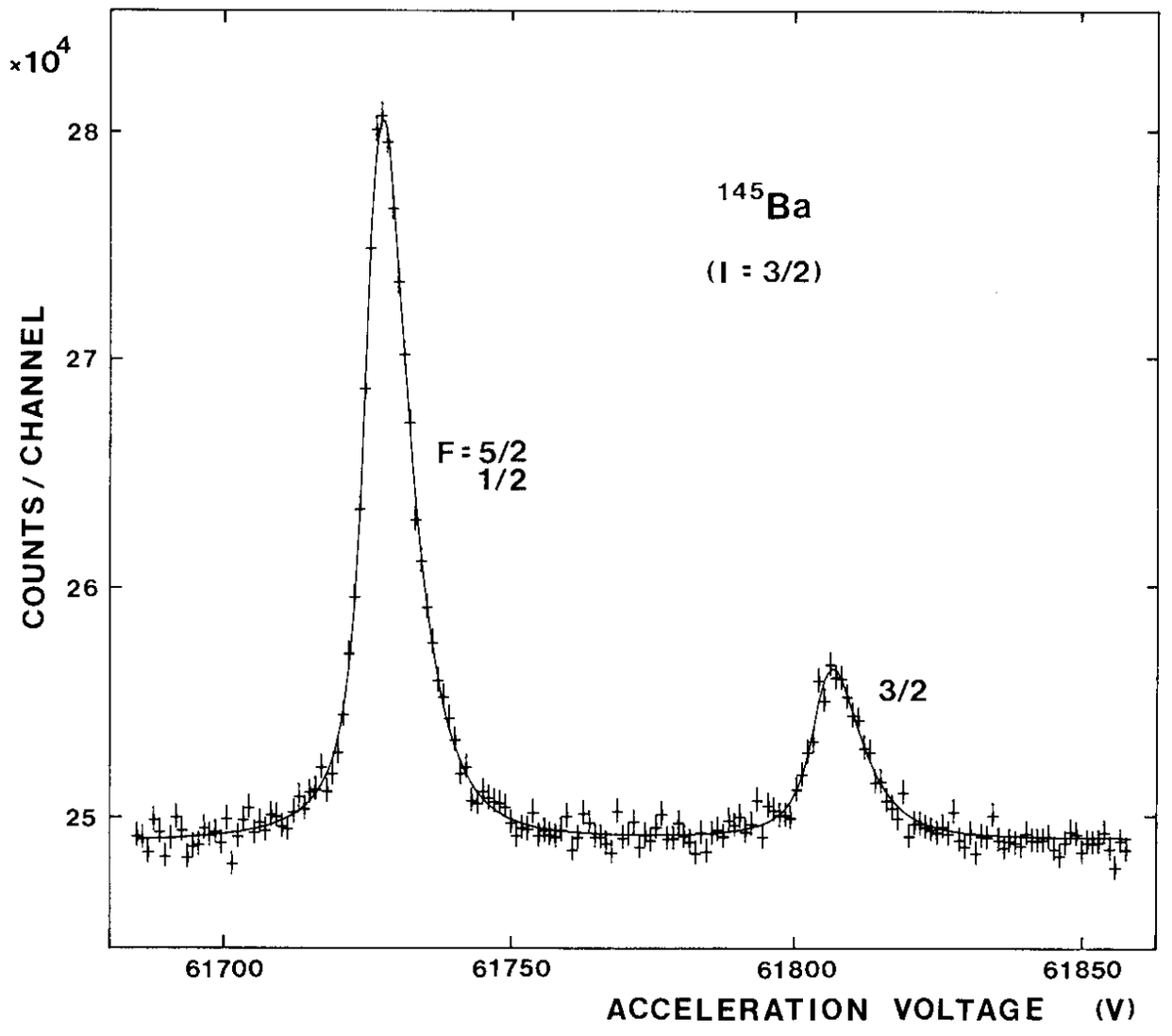
×10^4
28
27
26
25
COUNTS / CHANNEL
145Ba
(I = 3/2)
F = 5/2
1/2
3/2
61700
61750
61800
61850
ACCELERATION VOLTAGE (V)

Fig. 6

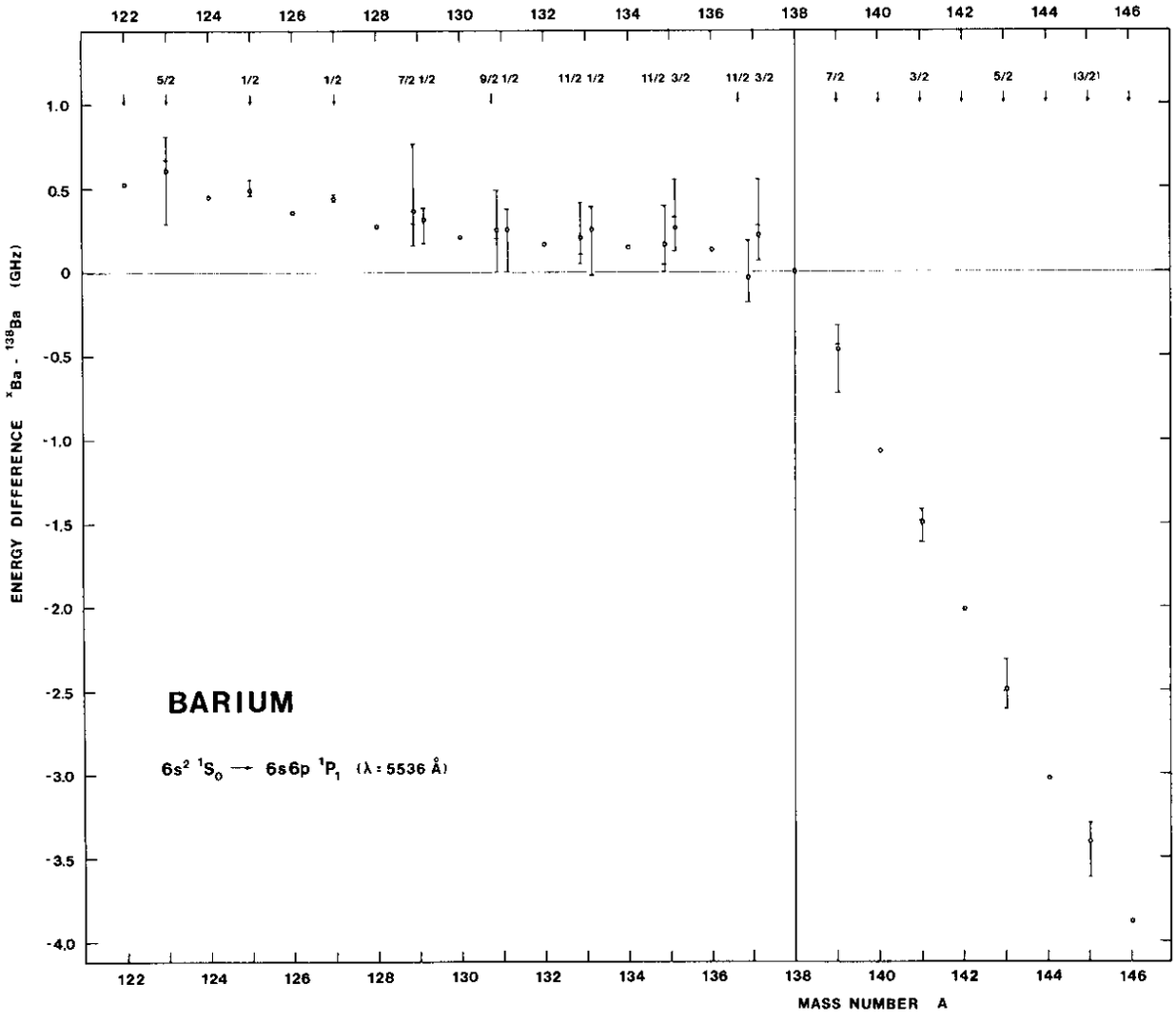
122 124 126 128 130 132 134 136 138 140 142 144 146
5/2 1/2 1/2 7/2 1/2 9/2 1/2 11/2 1/2 11/2 3/2 11/2 3/2 7/2 3/2 5/2 (3/2)
1.0 0.5 0 -0.5 -1.0 -1.5 -2.0 -2.5 -3.0 -3.5 -4.0
ENERGY DIFFERENCE ^{x}Ba - ^{138}Ba (GHz)
BARIUM
$6s^2\ ^1S_0 \rightarrow 6s6p\ ^1P_1$ (λ = 5536 Å)
MASS NUMBER A

Fig. 7

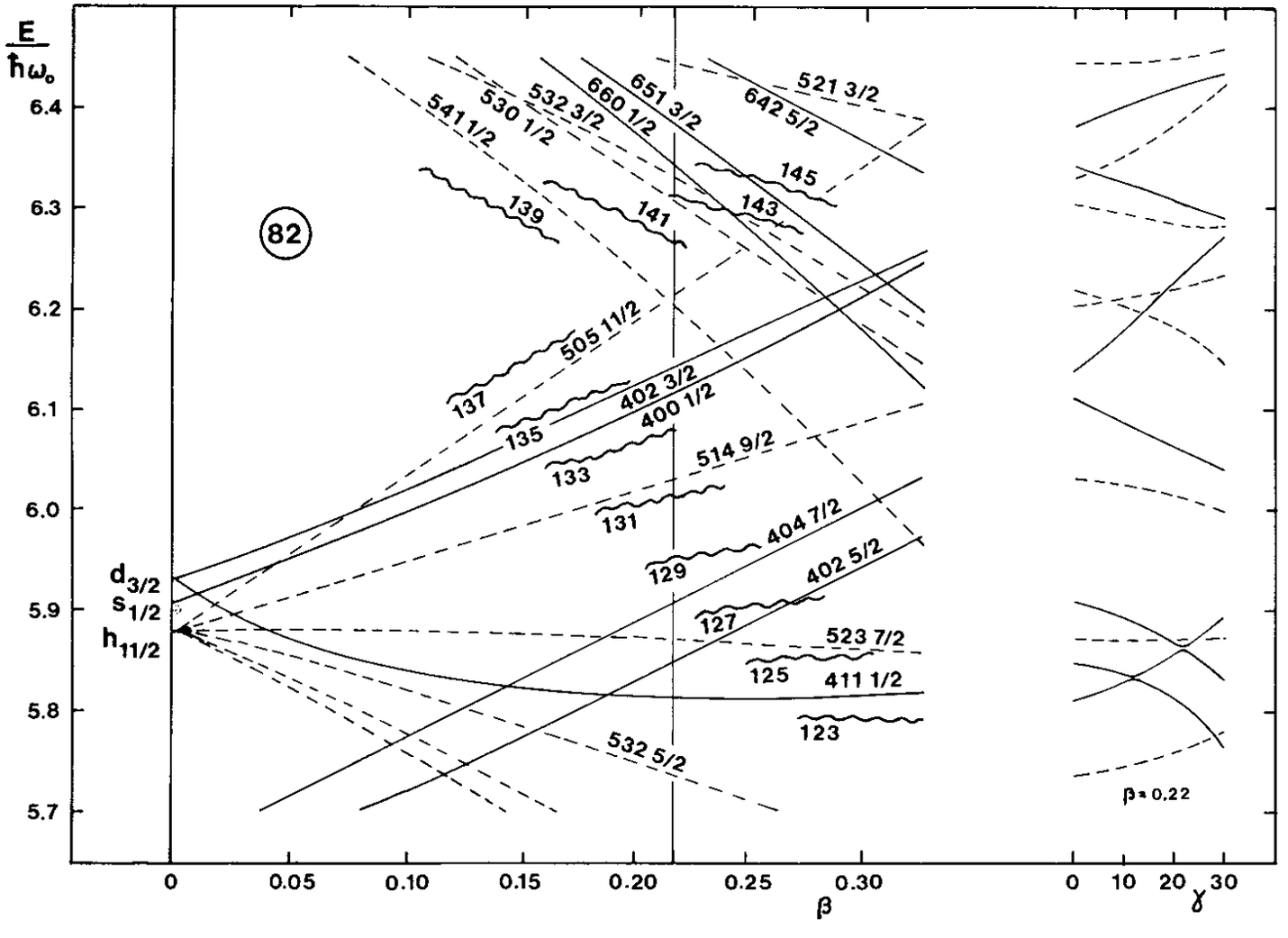
E/ħω₀
6.4
6.3
6.2
6.1
6.0
5.9
5.8
5.7
82
d3/2
s1/2
h11/2
541 1/2
530 1/2
532 3/2
660 1/2
651 3/2
642 5/2
521 3/2
139
141
143
145
505 11/2
137
402 3/2
135
400 1/2
133
514 9/2
131
404 7/2
129
402 5/2
127
523 7/2
125
411 1/2
123
532 5/2
β = 0.22
0
0.05
0.10
0.15
0.20
0.25
0.30
β
0
10
20
30
γ

Fig. 8

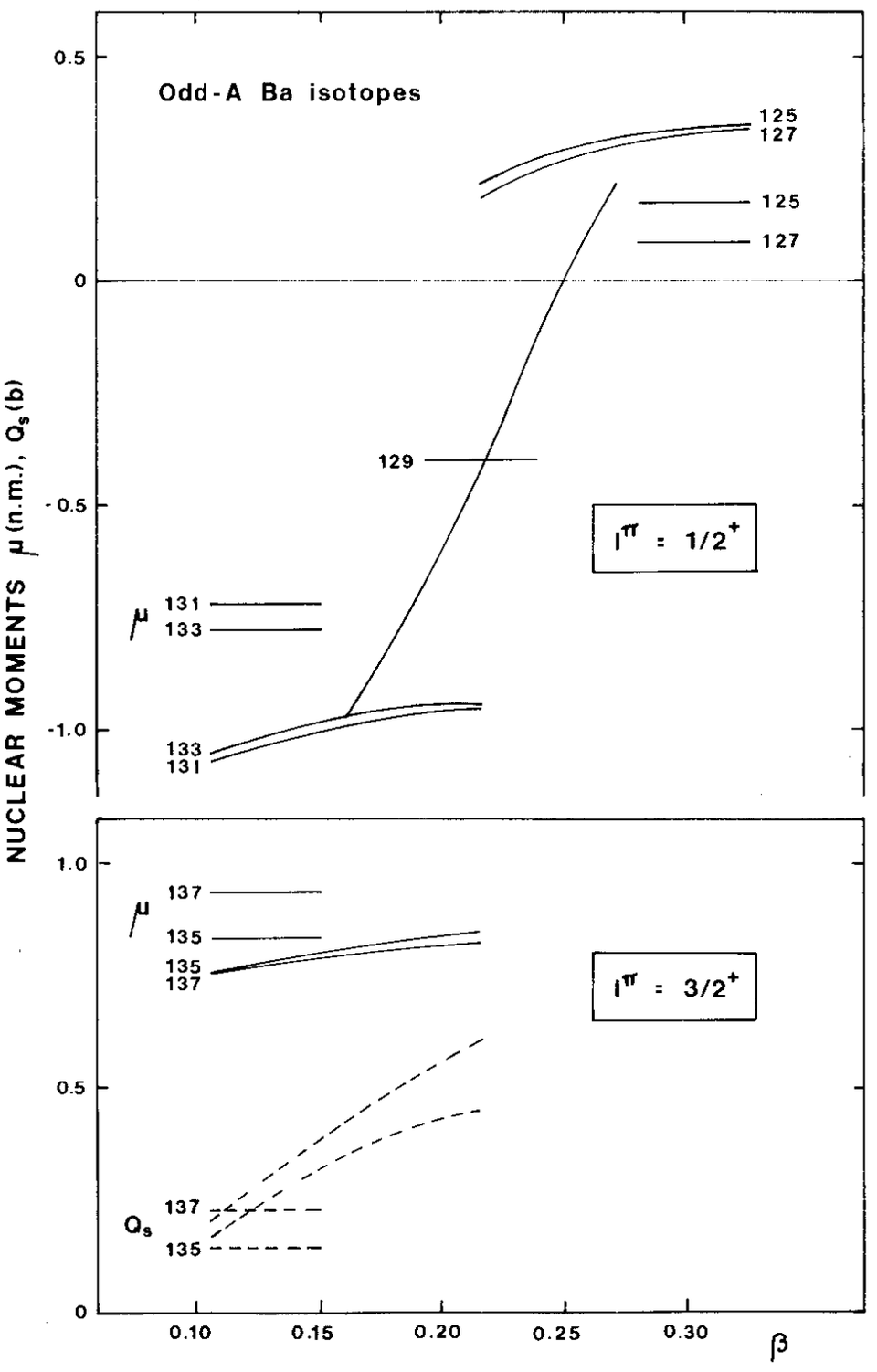
Odd-A Ba isotopes
NUCLEAR MOMENTS μ(n.m.), Q_s(b)
0.5
0
-0.5
-1.0
125
127
125
127
129
I^π = 1/2^+
μ
131
133
133
131
1.0
0.5
0
μ
137
135
135
137
I^π = 3/2^+
Q_s
137
135
0.10
0.15
0.20
0.25
0.30
β

Fig. 9

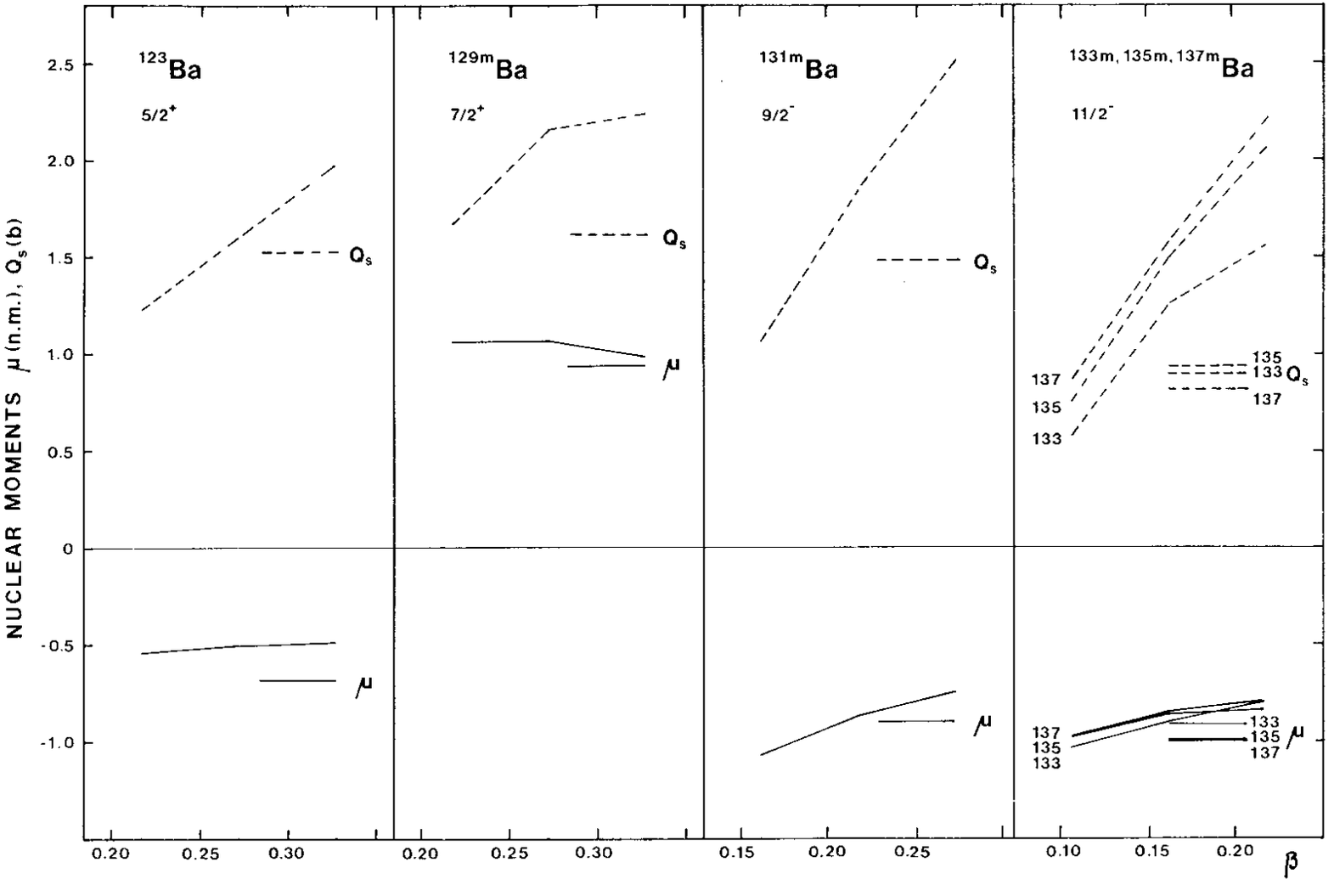
NUCLEAR MOMENTS μ (n.m.), Q_s (b)
123Ba
5/2+
129mBa
7/2+
131mBa
9/2-
133m, 135m, 137mBa
11/2-
Q_s
μ
137
135
133
β

Fig. 10

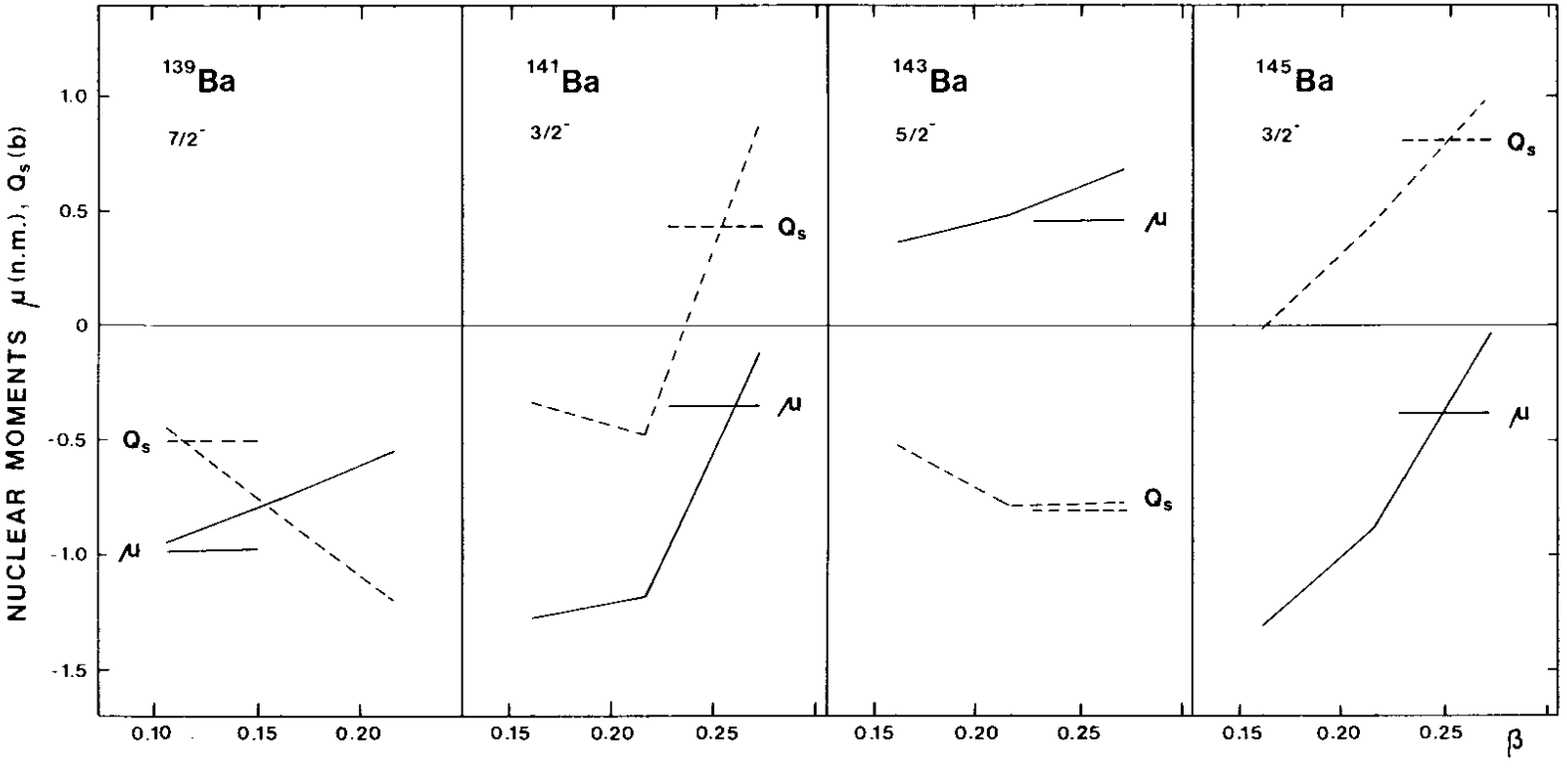
NUCLEAR MOMENTS μ (n.m.), Qs (b)
139Ba
7/2-
141Ba
3/2-
143Ba
5/2-
145Ba
3/2-
Qs
μ
1.0
0.5
0
-0.5
-1.0
-1.5
0.10
0.15
0.20
0.25
β

Fig. 11

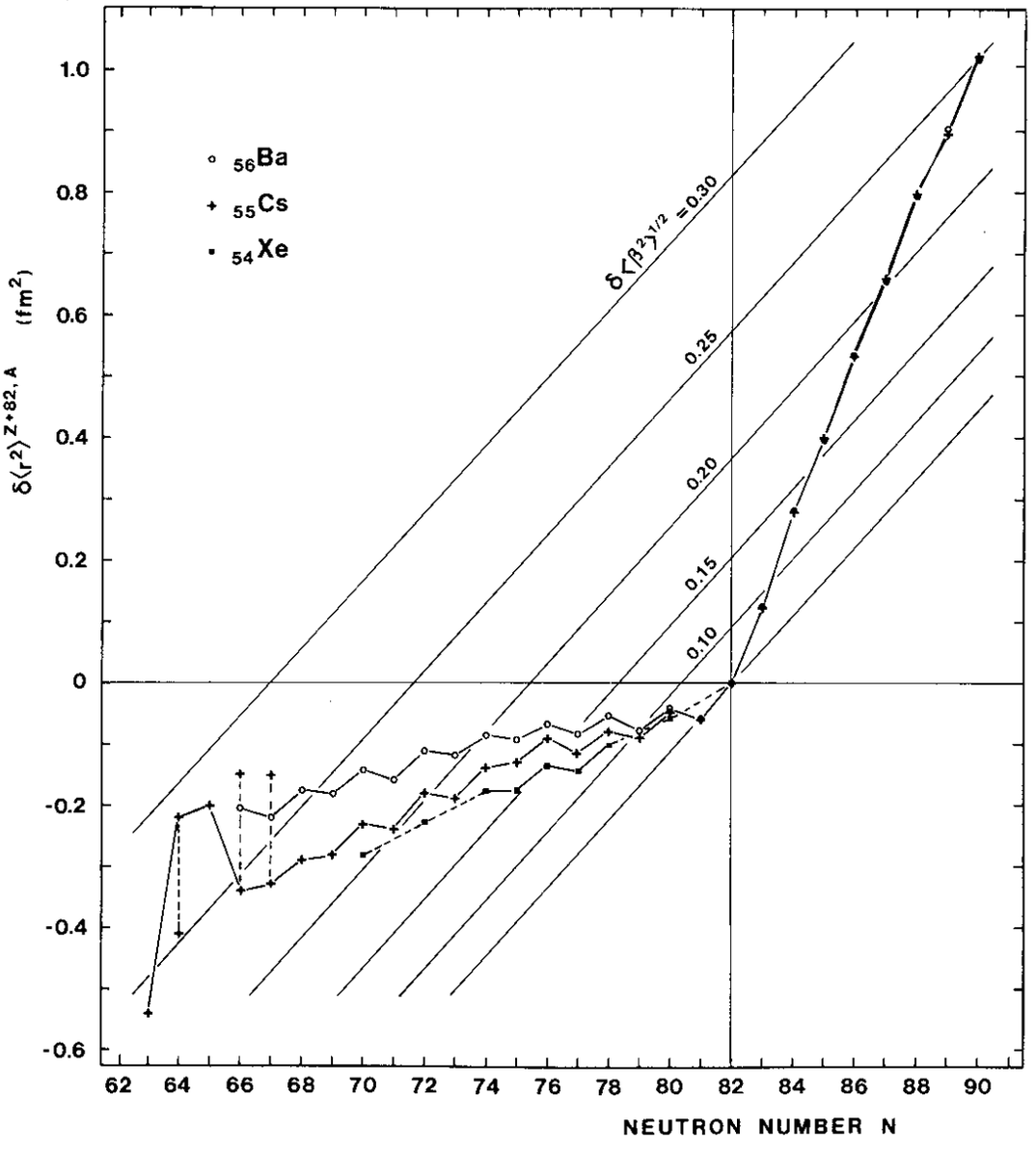
1.0
0.8
0.6
0.4
0.2
0
-0.2
-0.4
-0.6
62
64
66
68
70
72
74
76
78
80
82
84
86
88
90
NEUTRON NUMBER N
δ⟨r²⟩ Z·82, A (fm²)
56Ba
55Cs
54Xe
δ⟨β²⟩^1/2 = 0.30
0.25
0.20
0.15
0.10

Fig. 12

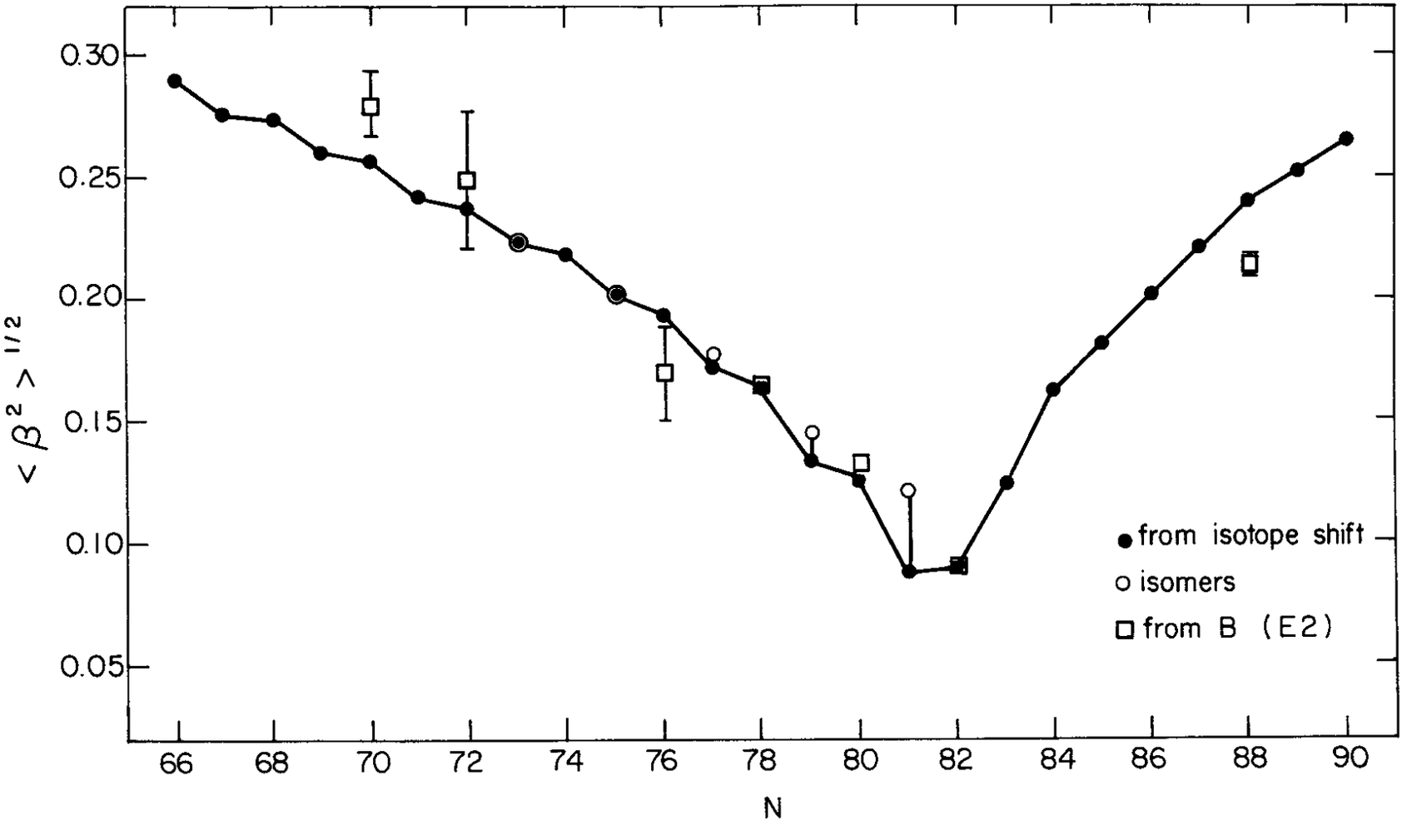
0.30
0.25
0.20
0.15
0.10
0.05
$< \beta^2 >^{1/2}$
66
68
70
72
74
76
78
80
82
84
86
88
90
N
● from isotope shift
○ isomers
□ from B (E2)

Fig. 13

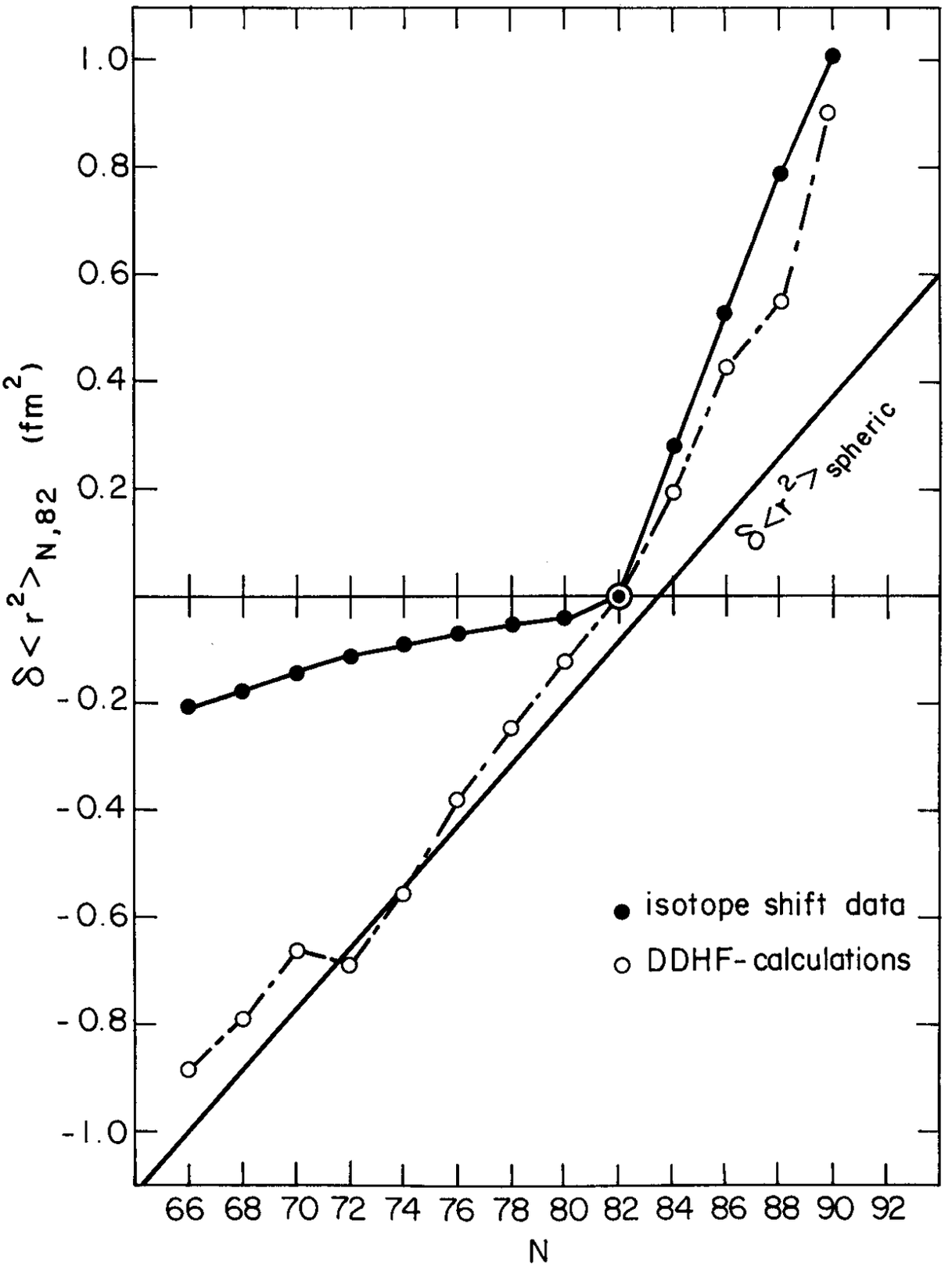
1.0
0.8
0.6
0.4
0.2
-0.2
-0.4
-0.6
-0.8
-1.0
$\delta\langle r^2\rangle_{N,82}$ (fm^2)
66 68 70 72 74 76 78 80 82 84 86 88 90 92
N
$\delta\langle r^2\rangle$ spheric
isotope shift data
DDHF-calculations

Fig. 14

E NUCLEAR STRUCTURE $^{122,123,125,127,131m,137m,139-146}$Ba; measured hyperfine constants A ($6s6p\,^1P_1$), B ($6s6p\,^1P_1$), spins, isotope shifts. Deduced μ, Q_s, r.m.s. charge radii, deformation β. Collinear fast-beam laser spectroscopy.